

1 **An ARGO and XBT observing system for the Atlantic Meridional Overturning**
2 **Circulation and Meridional Heat Transport (AXMOC) at 22.5°S**

3 **I. Pita^{1,2,3}, M. Goes^{2,3}, D. L. Volkov^{2,3}, S. Dong³, G. Goni³ and M. Cirano⁴**

4 ¹Rosenstiel School, University of Miami, Miami, FL, United States of America.

5 ²Cooperative Institute for Marine and Atmospheric Studies, University of Miami, Miami, FL,
6 United States of America.

7 ³Atlantic Oceanographic and Meteorological Laboratory, NOAA, United States of America.

8 ⁴Department of Meteorology, Institute of Geosciences, Federal University of Rio de Janeiro
9 (UFRJ), Brazil

10 Corresponding author: Ivenis Pita (ivenis.pita@noaa.gov)

11 **Key Points:**

- 12 • First in situ based Atlantic Meridional Overturning Circulation and Meridional Heat
13 Transport time series estimation at 22.5°S
- 14 • Mapping methodology used is robust and captures the climatological pattern for Atlantic
15 Meridional Overturning Circulation
- 16 • Western boundary system drives interannual Atlantic Meridional Overturning Circulation
17 variability, followed by eastern boundary system

18 Abstract

19 Changes in the Atlantic Meridional Overturning Circulation (AMOC) and associated Meridional
20 Heat Transport (MHT) can affect climate and weather patterns, regional sea levels, and
21 ecosystems. However, despite its importance, direct observations of the AMOC are still limited
22 spatially and temporally, particularly in the South Atlantic. The main goal of this study is to
23 implement a cost-effective trans-basin section to estimate for the first time the AMOC at 22.5°S,
24 using only sustained ocean observations. For this, an optimal mapping method that minimizes
25 the difference between surface in-situ dynamic height and satellite altimetry was developed to
26 retrieve monthly temperature and salinity profiles from Argo and XBT data along the 22.5°S
27 section. The mean AMOC and MHT for 22.5°S were estimated as 15.55 ± 2.81 Sv and 0.68 ± 0.18
28 PW, respectively, and are stronger during austral fall/winter and weaker in spring. The high-
29 resolution XBT data available at the western boundary are vital for capturing the highly variable
30 Brazil Current, and our section shows a significant improvement when compared to Argo
31 database. The mean values, interannual and seasonal time series of AMOC and MHT were
32 compared with other products. At 22.5S the North Atlantic Deep Water is divided into two cores
33 that flow along both western and eastern boundaries near 2500 m depth. Our results suggest a
34 greater influence of western boundary system on the AMOC variability at 22.5°S; highlight the
35 importance of high resolution in situ data for AMOC estimations; and contribute for a better
36 understanding of AMOC and MHT variability in the South Atlantic.

37 Plain Language Summary

38 The Atlantic Meridional Overturning Circulation (AMOC) is an ocean currents system
39 associated with large-scale meridional transport of heat (MHT) and nutrients that can modulate
40 climate, weather and ecosystems globally. In-situ measurements of the AMOC are still limited in
41 space and time, particularly in the South Atlantic. Previous studies used synthetic methodologies
42 based on statistical relationships between satellite sea surface height and in-situ temperature and
43 salinity profiles to calculate AMOC in different latitudes. However, these methodologies are
44 constrained by how good and stable these relationships are. Our new methodology obtains
45 monthly AMOC and MHT estimates at 22.5°S by gridding scattered profiles along a reference
46 section using optimal mapping parameters based on a sea level comparison to satellite data. The
47 methodology can resolve the western boundary current, westward propagating sea level features
48 and near coastal sea level variability. At 22.5°S the North Atlantic Deep Water is divided into
49 two southward cores along the western and eastern boundaries near 2500 m depth. The AMOC is
50 stronger during austral fall/winter and weaker in spring, and its interannual variability is linked
51 primarily to the western boundary current changes. This work provides evidence that an AMOC
52 monitoring section can be achieved by using solely sustained observations.

53 1 Introduction

54 The Atlantic Meridional Overturning Circulation (AMOC) is the zonal integral of the
55 complex three-dimensional circulation, characterized by an upper cell connected to the deep
56 convection in the North Atlantic subpolar region, and a lower or abyssal cell originated in the
57 marginal seas off Antarctica (Broecker, 2003; Buckley and Marshall, 2016). The AMOC controls
58 the distribution of heat and energy, tracers, and nutrients across the basin and links the timescales
59 of heat uptake and carbon storage (Conway et al., 2018; Collins et al., 2019; Todd et al., 2019).
60 The IPCC projections for the 21st century predict a significant weakening of the AMOC, which
61 if it happens, will result in global and regional impacts on climate, weather, sea level, and
62 ecosystems (Collins et al., 2019; Fox-Kemper et al., 2021; Lee et al., 2021). Theoretical and
63 climate models suggest that the stability of the AMOC is dependent on the oceanic freshwater
64 budget in the South Atlantic (de Vries & Weber, 2005; Stommel, 1961; Weijer et al., 2019).
65 Depending on the sign of the freshwater transport into the South Atlantic, the AMOC may
66 present a hysteresis behavior, in which a collapsed AMOC could be sustained even without an
67 anomalous freshwater forcing (Rahmstorf et al., 1996; Stommel, 1961). Because the net
68 freshwater transport across 35°S in the South Atlantic is southward (Garzoli et al., 2013), a
69 weakening of the AMOC would increase the freshwater transport into the Atlantic, causing
70 negative feedback to the AMOC recovery (Goes et al., 2019b). In addition, the AMOC is one of
71 the main sources of uncertainties in climate model projections (Bellomo et al., 2021), which
72 highlights the importance of sustained observational data for a more robust AMOC
73 predictability. Therefore, the monitoring, hindcasting, and future projections of the AMOC
74 variability are crucial for a better understanding of the Earth system dynamics.

75 Despite its importance, observations of the AMOC are still limited spatially and
76 temporally, particularly in the South Atlantic (Rhein, 2019). There are only two in situ observing
77 arrays of the AMOC in the South Atlantic: the TSAA/Tropical Atlantic Circulation and
78 Overturning - TRACOS (11°S; Hummels et al., 2015; Herrford et al., 2021) and the South
79 AMOC Basin-wide Array - SAMBA (35°S; Meinen et al., 2018; Kersalé et al., 2020). TRACOS
80 uses a total of 5 bottom pressure stations to capture boundary variability on both boundaries of
81 the Atlantic basin, combined with altimetry data to obtain AMOC anomalies at 11°S. Hummels
82 et al. (2015) detected a salinity increase of up to 0.1 psu per decade from the surface to
83 intermediate layers at 5°S and 11°S near the western boundary by comparing observations from
84 two periods, 2013-2014 and 2000-2004. Using reanalysis data, Goes et al. (2014) associated the
85 increase in salinity at intermediate depths to the increase of the salty Agulhas Leakage into the
86 Atlantic, due to the strengthening of the westerlies associated to the Southern Annular Mode,
87 similar to the mechanism described in Durgadoo et al. (2013). Herrford et al. (2021) observed an
88 important seasonal cycle in the AMOC variability, where in the upper 300 m the eastern
89 boundary forcing dominates the AMOC variability, but both eastern and western forcings are
90 important from 300 to 500 m depth.

91 At 35°S, SAMBA array has been in place since 2009, in the beginning with six PIES, and
92 over the years reaching more than twenty moorings, including two tall moorings deployed in
93 December 2022. This array revealed strong variability on both upper and abyssal cells of the
94 AMOC (Kersalé et al., 2020). The AMOC variability at 35°S is greatly influenced by the eastern
95 boundary forcing at an interannual time scale, but the western boundary contributions are still
96 significant (Meinen et al., 2018). The influence of the western boundary is greater on the AMOC
97 variability at semiannual or shorter time scales (Meinen et al., 2018). These results suggest a

98 greater influence of both boundaries on the AMOC dynamics in the South Atlantic when
99 compared to the North Atlantic.

100 Recent studies have stressed the need for understanding the meridional coherence of the
101 AMOC (e.g., Frajka-Williams, 2019; McCarthy et al., 2020). Anomalous signals from the South
102 Atlantic can propagate towards the subpolar North Atlantic and affect deep water formation
103 (Biaostoch et al., 2009; Desbruyeres et al., 2021). The AMOC-induced heat and freshwater
104 convergences and divergences drive changes in regional heat and freshwater contents and in sea
105 level (Little et al., 2017; Volkov et al., 2019), which can impact the climate locally (Chang et al.,
106 2008) and remotely (Lopez et al., 2016).

107 Building an AMOC observing system at 22.5°S will bridge the two existing observing
108 systems located at the edges of the South Atlantic subtropical gyre, and provide estimates that
109 can be compared to the historical cross-basin hydrographic programs such as WOCE and GO-
110 SHIP occurring since the early 1990s. However, building new, sustainable observing systems
111 can be a daunting task due to the operational and financial costs associated with it (Chidichimo et
112 al., 2023). Therefore, an AMOC observing system that can rely on existing sustained
113 observations at no additional costs is a strategic opportunity that will enhance our understanding
114 of this vital climate component.

115 Although there are altimetry-based AMOC reconstructions at a few locations in the South
116 Atlantic (e.g., Dong et al., 2021, Schmid et al., 2018), these estimates rely on linear regression
117 between altimetry and in situ data, which are dependent on the reliability of these relationships.
118 However, between 11°S and 35°S, an AMOC estimate which relies solely on sustained
119 hydrographic data has not been attempted previously. At 22°S, the existing AX97 XBT high-
120 density transect, which to date accounts for nearly 100 sections, can be a reliable constraint of
121 the variability of the western boundary current, which is known to have a great influence on the
122 AMOC variability in other locations (e.g., Gulf Stream). In addition, according to Dong et al.
123 (2021), the AMOC time series at 35°S is not correlated with 20°S, which suggests a different
124 regime than the current existing arrays, thus the 22°S estimate can serve as a benchmark for the
125 AMOC variability in this latitude.

126 With that said, we implement a cost-effective transbasin section at 22.5°S to estimate the
127 AMOC and its seasonal and interannual variability over 2007-2020 by merging available in situ
128 observations and reanalysis products.

129 This paper is organized as follows: the in situ and reanalysis data used in this study are
130 presented in Section 2, as well as the methodology to construct the referenced transect and its
131 AMOC estimation. Section 3 consists in evaluating the methodology. Section 4 presents the
132 AMOC and Meridional Heat Transport (MHT) time series, and their different components from
133 the reference section and from other products available in the region. Section 5 gives a summary
134 of the present study.

135 **2 Data and Methods**

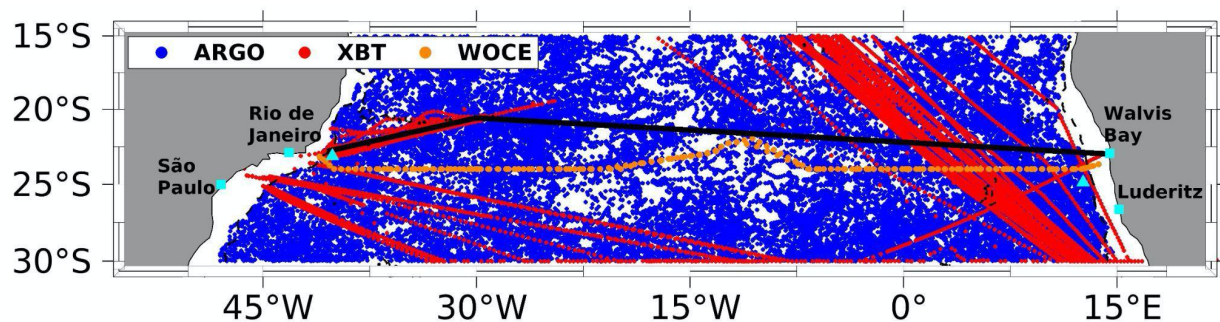
136 **2.1 In-situ profile data**

137 Observational data from three high density expendable bathythermograph (XBT)
138 transects (AX08, AX18 and AX97) and Argo profiling floats in the South Atlantic Ocean are
139 used to build a transbasin transect near 22.5°S (Figure 1). The XBT probes measure temperature

140 (T) along fixed transects from surface to depths of about 800 m, and Argo floats measure T and
 141 salinity (S) down to 2000 m. The AX08 transect crosses the Atlantic Ocean from Cape Town
 142 (South Africa) to New York (USA), spanning through the eastern part of the South Atlantic
 143 subtropical gyre. The AX18 transect monitors the AMOC and MHT with two cross-basin zonal
 144 transects at approximately 34.5°S, and some of its realizations go further north to ~24°S in the
 145 western side of the basin depending on the availability of merchant ships. The AX97 monitors
 146 the BC at 22°S from Rio de Janeiro (Brazil) to Trindade Island (~30°W). The average temporal
 147 sampling frequency of AX08 and AX18 transects is 3 months/year and 2 months/year for the
 148 AX97. The average horizontal resolution ranges from 18 to 27 km. T data from XBT probes are
 149 obtained from the NOAA/AOML database. S profiles are derived from XBT-based T profiles
 150 using a seasonal regression method proposed by Goes et al. (2018). Delayed mode Argo profile
 151 data (Argo 2020) are used from the Global Argo Data Repository of the National Centers for
 152 Environmental Information (NCEI). Only Argo T-S profiles flagged as good or potentially good
 153 are used. The disparity found in some profiles, for which the available S data were fewer than the
 154 T data, was circumvented by applying the same regression methodology to estimate S for the
 155 XBT profiles.

156 To complete the profiles for the full water column, i.e., below 800 m for XBT data and
 157 below 2000 m for Argo data, the 0.25° horizontal resolution NCEI World Ocean Atlas 2018
 158 (WOA18) T-S climatology is used, at monthly averages between 800 and 1500 m, and seasonal
 159 averages below 1500 m (Garcia et al., 2019; Locarnini et al., 2018; Zweng et al., 2018). Monthly
 160 WOA18 data have 57 vertical levels from 0 to 1500 m, and seasonal data have 112 vertical levels
 161 from 0 to 5500 m. Sensitivity tests performed with Argo data showed that the effect of padding
 162 from 800-1600 m is negligible relative to uncertainties that arise from the sampling strategies
 163 and from the methodologies of heat and volume transports calculation.

164 Each T-S profile is linearly interpolated to 140 pre-defined depths, starting from 5 m at
 165 10 m intervals until 750 m, 50 m intervals until 2000 m, and 100 m intervals until a maximum
 166 depth of 6000 m.



167

168 **Figure 1.** Spatial distribution of in situ data used in this work. Location of Argo (XBT) profilers
 169 are represented by blue (red) dots, and yellow dots represent the location of T-S profilers
 170 acquired at WOCE cruises in 2009 and 2018. The reference transect is represented by the black
 171 line. The location of coastal tide gauges is represented by cyan squares. Cyan triangles represent

172 the coordinates of sea level data from altimetry dataset compared to AXMOC data at the
173 boundaries. Dashed black lines represent the 1000 m isobath.

174 2.2 Auxiliary data

175 To estimate the Ekman component of the AMOC, we use the monthly zonal wind stress
176 from the ERA5 atmospheric reanalysis (Hersbach et al., 2020), which is available at a 0.25°
177 horizontal grid since 1979. We linearly interpolated ERA5 wind stress to the reference section
178 for the period 2007-2020.

179 For data validation, comparison, and water mass analysis, we used the Argo T-S 0.5° x
180 0.5° gridded monthly climatology (RG Argo- Roemmich & Gilson, 2009) from 2007-2020, and
181 the World Ocean Circulation Experiment (WOCE) hydrographic profiles (Koltermann et al.,
182 2011). The WOCE T-S data from transect A9.5 located close to 24°S from South America to
183 Africa were acquired by two different scientific cruise surveys in 2009 and 2018
184 (740H20090307 and 740H20180228, respectively). A total of 238 CTD/O₂ stations were
185 collected in those 2 periods, and 214 of those stations were used in this study (Figure 1). WOCE
186 data are interpolated to the same 140 pre-defined depths used in the XBT and Argo profiles.
187 WOCE data are used as independent measurements to evaluate the methodology adopted by this
188 study in obtaining high-resolution T-S sections at 22.5°S. We also used the T-S from ECCO
189 version 4 release 4 (ECCOv4r4), covering the period 1992-2017 at a 0.5° x 0.5° horizontal
190 resolution. This product is an updated edition to that described by Forget et al. (2015). Finally,
191 for the in situ profile data mapping calibration and validation, we use monthly gridded sea level
192 anomaly (SLA) from January 1993 to December 2020 from a multi-satellite altimetry mission,
193 processed and distributed by the Copernicus Marine and Environment Monitoring Service
194 (CMEMS). The SLA maps are filtered, bias corrected, and corrected for atmospheric pressure
195 effects and tides using the method of Pujol et al. (2016). Monthly maps of a 20-yr mean dynamic
196 topography (Rio et al., 2011) are added to SLA to obtain the sea surface height (SSH) fields. The
197 global mean sea level rose on a rate of $3.35 \pm 0.4 \text{ mm yr}^{-1}$ from 1993 to 2017 (Ablain et al.,
198 2019), which was $\sim 1.95 \text{ mm yr}^{-1}$ higher than the calculated in situ dynamic height (DH) trends.
199 To avoid time varying biases during the mapping optimization phase, linear trends are removed
200 from the fields at each longitude of the reference transect.

201 2.3 High-Resolution T-S Reference Section mapping methodology

202 A high-resolution reference section based on Argo and XBT data at 22.5°S, hereafter
203 AXMOC, was defined in order to maximize the data availability along the section. Therefore, on
204 the western side of the basin, the section follows the AX97 XBT transect from Rio de Janeiro to
205 Trindade Island ($\sim 30^\circ\text{W}$), and from 30°W to Walvis Bay in Namibia. Long-record tide gauges
206 are located on both ends of the reference transect (Figure 1). Data from two other XBT transects,
207 the AX08 and AX18 are used to improve data coverage locally along their tracks. The coverage
208 of Argo profiles is greater where bathymetry is deeper than 1000 m, and it has improved after
209 2007 in the South Atlantic following the initial spinup of the program since 2004 (Roemmich et
210 al., 2009).

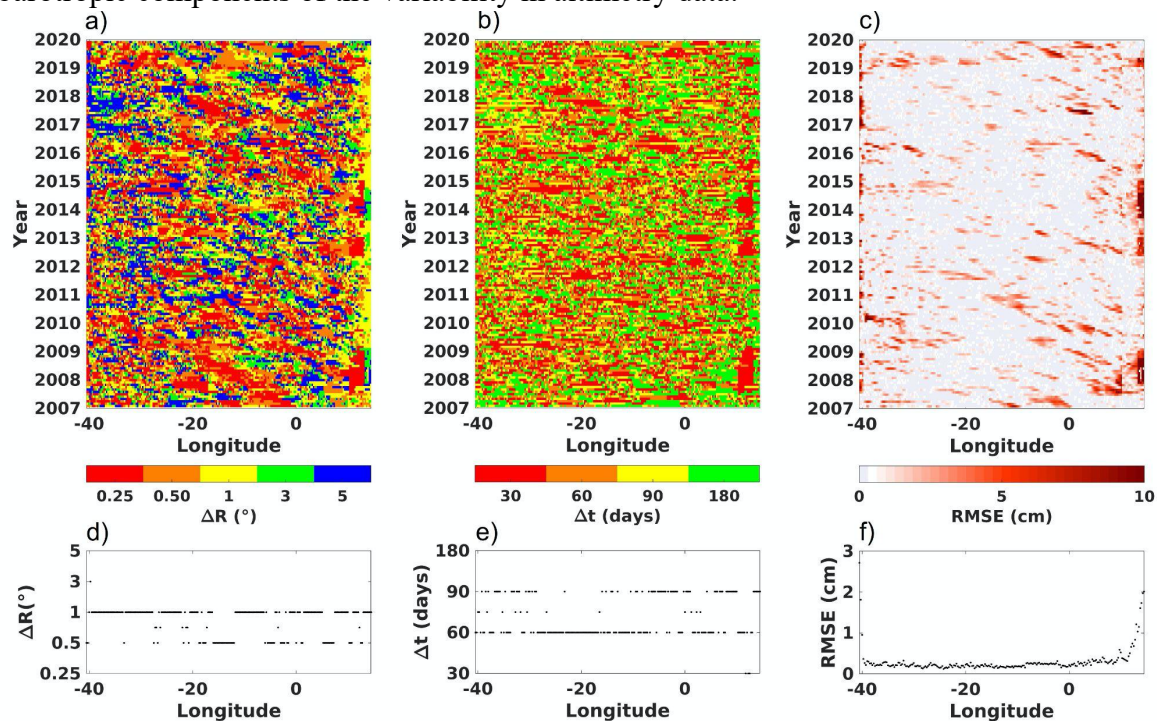
211 The mapping methodology used to reconstruct the reference section consists in weighted
212 averages (Goes et al., 2010; Goes et al., 2020) using a normalized separable exponential function
213 in space and time, given by:

214

$$W = \exp\left(-\frac{\sqrt{x^2+y^2}}{\Delta R}\right) * \exp\left(-\frac{\delta t^2}{\Delta t}\right) \quad (1),$$

215 where ΔR is a spatial radius, Δt is a time window, δt is the time difference between the profile
 216 and the reference time (15th of each month), and x and y are the zonal and meridional distance
 217 between the profile location and the referenced coordinate position, respectively. A set of 20
 218 reference sections is generated considering a combination of weight values obtained varying ΔR
 219 (0.25°, 0.50°, 1°, 3° and 5° radius) and Δt (30, 60, 90 and 180 days). The search radius at the
 220 boundaries (<30°W and >0°) are enlarged in the y-direction by a factor of 3 with a cut off of 5°
 221 in order to minimize data gaps, assuming the features are more coherent along the boundaries
 222 than across.

223 The optimal T-S section is obtained by optimizing the mapping parameters ΔR and Δt
 224 locally by reducing the root mean squared error (RMSE; used as a cost function) between
 225 absolute DH and the SSH data interpolated to the reference section (Figure 2). The absolute DH
 226 of each parameter subset is referenced to 1000 m, and the absolute geopotential field from a
 227 blended Argo/altimetry climatology product is added to the reference level, similar to Goes et al.
 228 (2019). During calibration, both data are detrended in time to avoid misfits due to the mass and
 229 barotropic components of the variability in altimetry data.



230

231 **Figure 2.** Values of spatial (a) and temporal (b) ranges used on the optimized mapping
 232 methodology to minimize the Root Mean Square Error (c). Median values for each longitude are
 233 presented for spatial range (d), temporal range (e) and RMSE (f).

234 The optimal ΔR and Δt parameter selection is generally noisy (Figure 2), which reflects
 235 the variable data coverage along the section, suggesting that small differences in the RMSE can
 236 influence the choice of the mapping parameters, and contribute to this variability. A possible
 237 solution to this issue is to include a prior probability distribution in the parameters to prioritize
 238 ΔR and Δt with higher resolution when RMSE variability is small among the different

239 parameters (e.g., Goes et al., 2010). From sensitivity experiments, the impact of this approach in
240 the final AMOC and MHT time series is small, even for higher ΔR and Δt values, since our
241 methodology guarantees that greater weight is given to data closer in time and space to the
242 referenced transect at a given time (Equation 1). The median ΔR (Δt) values fall between 0.50°
243 and 1° (60 and 90 days) for every point of latitude (Figure 2d-e). Therefore, the median RMSE
244 value between absolute HD and SSH is 0.79 ± 1.40 cm, and increases to ~ 2 cm in the eastern
245 boundary (Figure 2f). These values fall well within previously published RMSE values of 6.2 cm
246 for areas between 5°S and 15°S , and up to 14 cm at the boundaries (Arnault et al., 1992; Strub et
247 al., 2015).

248 2.4 AMOC and MHT time series

249 The AMOC and MHT across the reference section are calculated following published
250 methodologies for the South Atlantic (e.g., Dong et al., 2015, 2021; Goes et al., 2015, 2020). The
251 AMOC and MHT are divided into geostrophic and Ekman components. The geostrophic velocity
252 field is computed from the gridded T-S data, using 3700 m as reference level, since it is
253 approximately the depth of the neutral density $\gamma = 28.1$ kg/m³, usually considered as the boundary
254 between North Atlantic Deep Water (NADW) and Antarctic Bottom Water (AABW) at 22.5°S
255 (see Section 3.3). This reference depth is similar to the one defined for 34.5°S (Goes et al.,
256 2015). A zero net volume transport constraint is applied to the section at each month by adjusting
257 the velocity field with a constant, calculated from the integrated transport across the section
258 divided by the area of the section. The geostrophic AMOC streamfunction is estimated from the
259 adjusted velocities, and its strength is defined as the maximum streamfunction at each timestep.
260 The geostrophic time series is smoothed with a 3-month low-pass gaussian filter in order to
261 remove high-frequency signals. The Ekman component, estimated using the ERA5 reanalysis, is
262 integrated to the depth of the Ekman layer, which is considered to be 50 m deep. Both the
263 AMOC and MHT represent the sum of Ekman and geostrophic components. The time series of
264 the AMOC and MHT span from 2007 to 2020, since the AX97 transect started in 2004 and the
265 Argo data has been more widely available across the South Atlantic basin after 2007.

266 3 Results

267 In this section, sea level, boundary currents, and water mass characterization are
268 presented to evaluate the AXMOC product. The AMOC and MHT time series are decomposed
269 into the seasonal, interannual (low-pass filtered with a 13-month Gaussian), as well as Ekman
270 and geostrophic components.

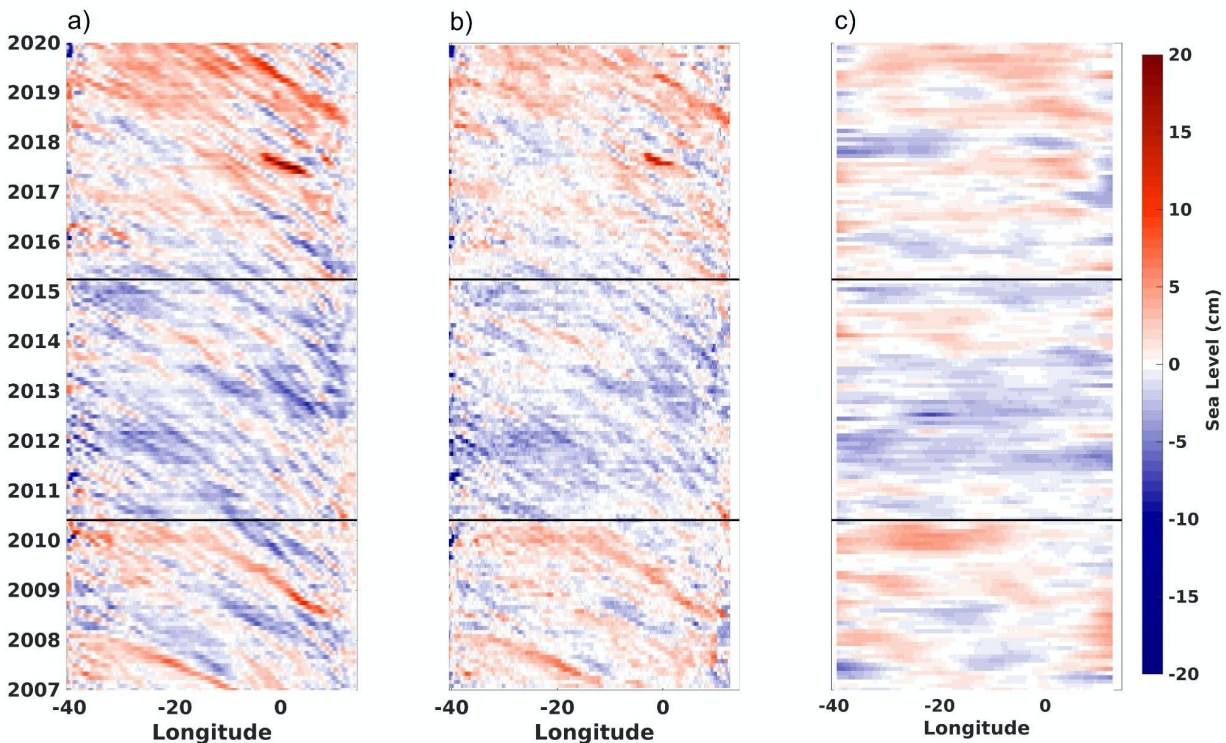
271 3.1 Sea level

272 Here, the SLA calculated along the AXMOC transect from 2007 to 2020 is compared
273 with the ones obtained from satellite altimetry and from the RG Argo data (Figure 3). Westward
274 propagating signals are observed in satellite altimetry. These signals take between 2 to 4 years to
275 cross the basin from east to west, generally without significant energy loss along their path,
276 showing the importance of wave generation near the eastern boundary. An average phase speed
277 of 5.9 ± 1.6 km/day is estimated for these propagations following the method of Barron et al.
278 (2009), which corresponds to the period of the 1st baroclinic Rossby wave mode near 22.5°S
279 (Polito and Liu, 2003). This westward propagation is not seen in the RG Argo product due to a
280 rather coarse spatial and temporal mapping resolution. Nevertheless, our optimized mapping

281 methodology calibrated to the SLA altimetry data allows detecting these propagation patterns
 282 reliably, in a good agreement with satellite altimetry data (Figure 3a, b).

283 A basin-wide, multi-year SLA pattern is observed in all three products, characterized by
 284 positive anomalies from 2007 to Jun/2010, negative between Jun/2010 and Apr/2015, and again
 285 positive from Apr/2015 to Dec/2020. As this variability pattern is characteristic for the entire
 286 basin, it could be linked to large-scale climate modes.

287 The proposed mapping methodology (AXMOC) also adequately reproduces the strong
 288 SLA variability near the boundaries, particularly near the western boundary due to the higher
 289 density of XBT data in the region. Near the eastern boundary, both satellite altimetry and
 290 AXMOC products capture some strong SLA signals, such as the negative anomalies in 2012-
 291 2013 and the positive anomalies in 2008-2009, 2017 and 2018-2019.

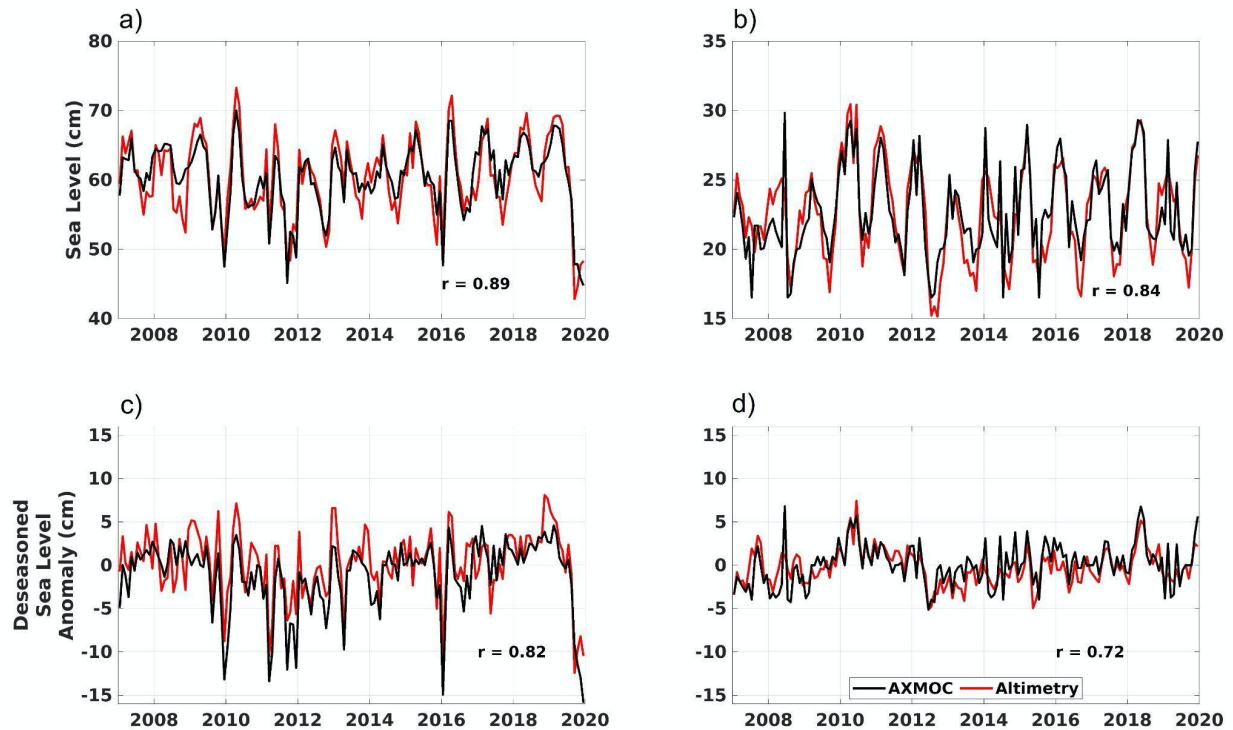


292

293 **Figure 3.** Hovmoller plot of the sea level obtained by altimetry (a), AXMOC (b) and RG Argo
 294 (c) datasets. Black horizontal lines indicate dates of 06/2010 and 04/2015. All datasets are de-
 295 seasoned and detrended to focus on the interannual variability.

296 The comparison of SLA time series from satellite altimetry and the AXMOC data near
 297 the western (40°W) and eastern boundaries (12.5°E) also validates the proposed methodology
 298 and provides valuable insight of the boundary currents variability (Figure 4). Since satellite SSH
 299 has other contributions than steric sea level, particularly in coastal areas, we selected for the
 300 boundary sea level height comparison with AXMOC the location of the satellite altimetry time
 301 series with higher correlation within 3° from the boundaries. The selected locations for the
 302 altimetry product are 40.12°W , 23.12°S (western boundary), and 12.62°E 24.87°S (eastern
 303 boundary), shown in light blue triangles in Figure 1. Overall, the region near the western
 304 boundary has greater variability compared to the eastern boundary (Figure 4). The standard
 305 deviation (used as a proxy of variability) of the SSH near the western boundary was 5.7 cm

306 (Figure 4a), and 3.4 cm (Figure 4b) near the eastern boundary. The AXMOC data show similar
 307 values to SSH near the western (4.9 cm) and eastern (3.1 cm) boundaries.



308

309 **Figure 4.** Absolute (a and b) and de-seasoned (c and d) SSH at the western (a and c) and eastern
 310 (b and d) boundaries of the section. Red is for altimetry data, and black is for the AXMOC
 311 estimates. The associated correlation values are shown in each panel.

312 A good correlation of sea level from AXMOC with altimetry data was obtained at both
 313 boundaries (0.89 at the western and 0.84 at the eastern boundary). When considering the de-
 314 seasoned sea level anomaly, the correlation at both boundaries remained robust (0.82 for the
 315 western and 0.72 for the eastern boundary). Most of the SLA extreme events that arise in the
 316 altimetry data also appeared in the AXMOC data (e.g., extreme values at the end of 2009, 2011,
 317 2016, and end of 2019 at the western boundary, and the extreme values early 2010, mid 2012 and
 318 mid 2018 at the eastern boundary). The robust correlations observed on both ends of the section,
 319 even though the western boundary is densely sampled by XBTs and the eastern boundary is only
 320 sparsely sampled by Argo floats, indicate that the use of a sea level-oriented mapping
 321 methodology is appropriate to monitor the evolution of near-coastal features.

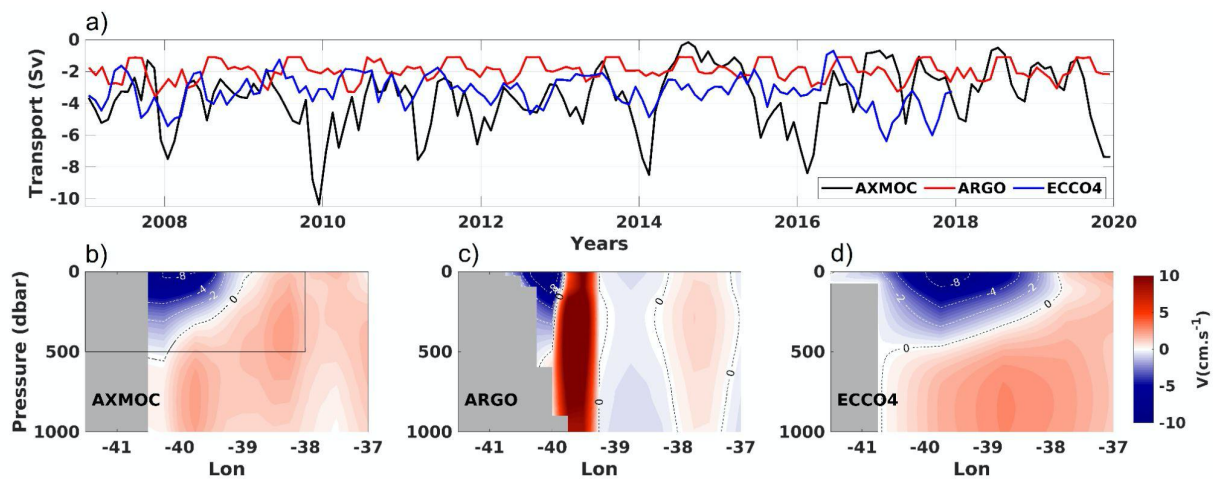
322

3.2 Boundary currents

323

324 Here, we compare boundary currents derived from the AXMOC with those derived from
 325 the RG Argo and simulated by the ECCOV4r4 state estimate. At 22.5°S , the BC is a shallow and
 326 narrow southward flow along the Brazilian coast placed on top of the northward inflow of the
 327 Intermediate Western Boundary Current (Calado et al., 2008). In the AXMOC data, the mean BC
 328 is located west of 39°W in the top 500 m (Figure 5). In the RG Argo, the BC is constrained to the
 329 west of 39.75°W , and a strong northward core appears east of 39.75°W , which is an artifact
 330 caused by the reverse DH gradient created from the lack of in situ data near the western
 boundary (Goes et al., 2020). In ECCOV4r4, the BC appears shallower and wider (west of 38°W)

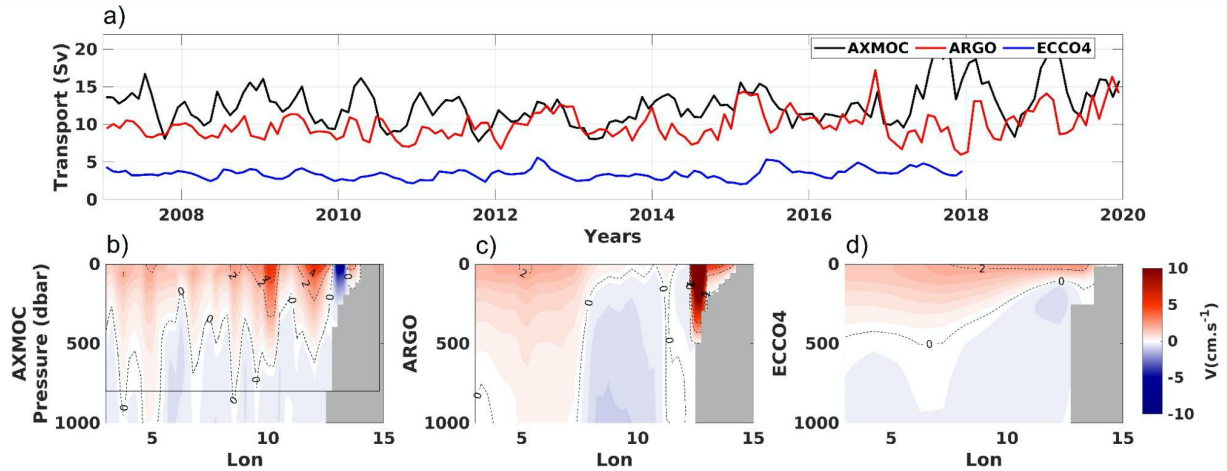
331 than in the AXMOC data. To analyze its volume transport in the three data products, we define
 332 the BC as the southward flow in the upper 500 m between the western boundary and 38°W. The
 333 10-year (2007 to 2017) averaged and standard deviation of the volume transport is higher ($-$
 334 3.74 ± 1.92 Sv) for the AXMOC, compared to -1.95 ± 0.62 Sv for the RG Argo and -3.23 ± 1.03 Sv
 335 for the ECCOV4r4. The mean BC core speed is also higher in the AXMOC data (-0.19 ± 0.10
 336 $m s^{-1}$) than in the RG Argo ($-0.15 \pm 0.04 m s^{-1}$) and ECCOV4r4 data ($-0.10 \pm 0.02 m s^{-1}$). The
 337 BC transport mean and standard deviation are better represented by AXMOC data when
 338 compared to previous regional studies (e.g., da Silveira et al. 2008; Lima et al., 2016; Mata et al.,
 339 2012; Pereira et al., 2014; Pita et al., 2020). This increased variance of the AXMOC is caused by
 340 a stronger BC interannual variability, which captures the strong event in the summer of
 341 2009/2010, analyzed in Goes et al. (2019), as well as other events such as 2014 and 2016 which
 342 were also observed in that study. This interannual variability is dampened in the other two
 343 products.



344

345 **Figure 5.** Evolution of the Brazil Current (BC) transport from 3 different data (a): AXMOC
 346 (black line), RG Argo (red line) and ECCOV4r4 (blue line). Mean velocity section focused on
 347 western boundary is shown for AXMOC (b), RG Argo (c) and ECCOV4r4 (d) datasets. The
 348 black rectangle indicates the region where the BC transport is being calculated.

349 Close to 22°S, the Benguela Current (BeC) is the eastern boundary current, which flows
 350 equatorward between the coast to 3°E, limited by the Walvis ridge (Garzoli et al., 1996;
 351 Majumder and Schmid, 2018). The AXMOC data capture the BeC as an equatorward flow from
 352 surface down to 500 m with a core located between 10 and 12°E (Figure 6). The poleward flow
 353 east of 12°E is the expression of the Poleward Undercurrent (PU), an ocean current derived from
 354 the sinking of the Angola Current at the Angola Benguela Frontal Zone (ABFZ - Berger et al.,
 355 1998). On the other hand, the RG Argo data shows a strong equatorward flow along the edge of
 356 continental shelf, due to the lack of data near the coast. The BeC transport of 12.57 ± 2.58 Sv
 357 observed in AXMOC is greater than the ones in the RG Argo (9.99 ± 1.95 Sv) and ECCOV4r4
 358 data (3.43 ± 0.68 Sv). AXMOC data perceive a more intense and variable BeC if compared to
 359 other products. The ECCOV4r4 estimate of BeC transport is lower than the AXMOC and RG
 360 Argo data. The ECCOV4r4 data capture a smoother BeC, with smaller interannual variability.
 361 The AXMOC results are in accordance with Majumder and Schmid (2018), which also reported
 362 a decreasing mean BeC volume transport on lower latitudes, varying from 23 Sv at 31°S to
 363 approximately 9 Sv at 25°S.

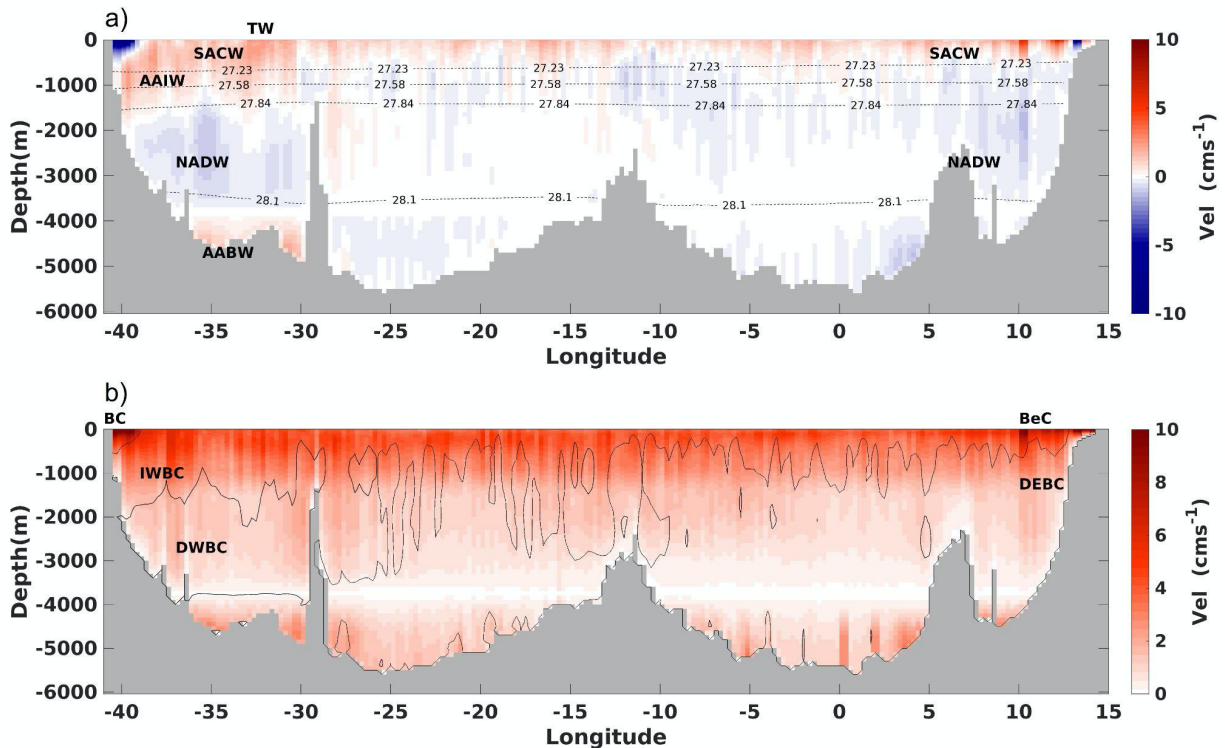


364

365 **Figure 6.** Evolution of the Benguela Current (BeC) transport from 3 different data (a): AXMOC
 366 (black line), RG Argo (red line) and ECCOv4r4 (blue line). Mean velocity section focused on the
 367 eastern boundary is shown for AXMOC (b), RG Argo (c) and ECCOv4r4 (d) datasets. The black
 368 rectangle indicates the region where the BeC transport is being calculated.

369 **3.3 Water masses**

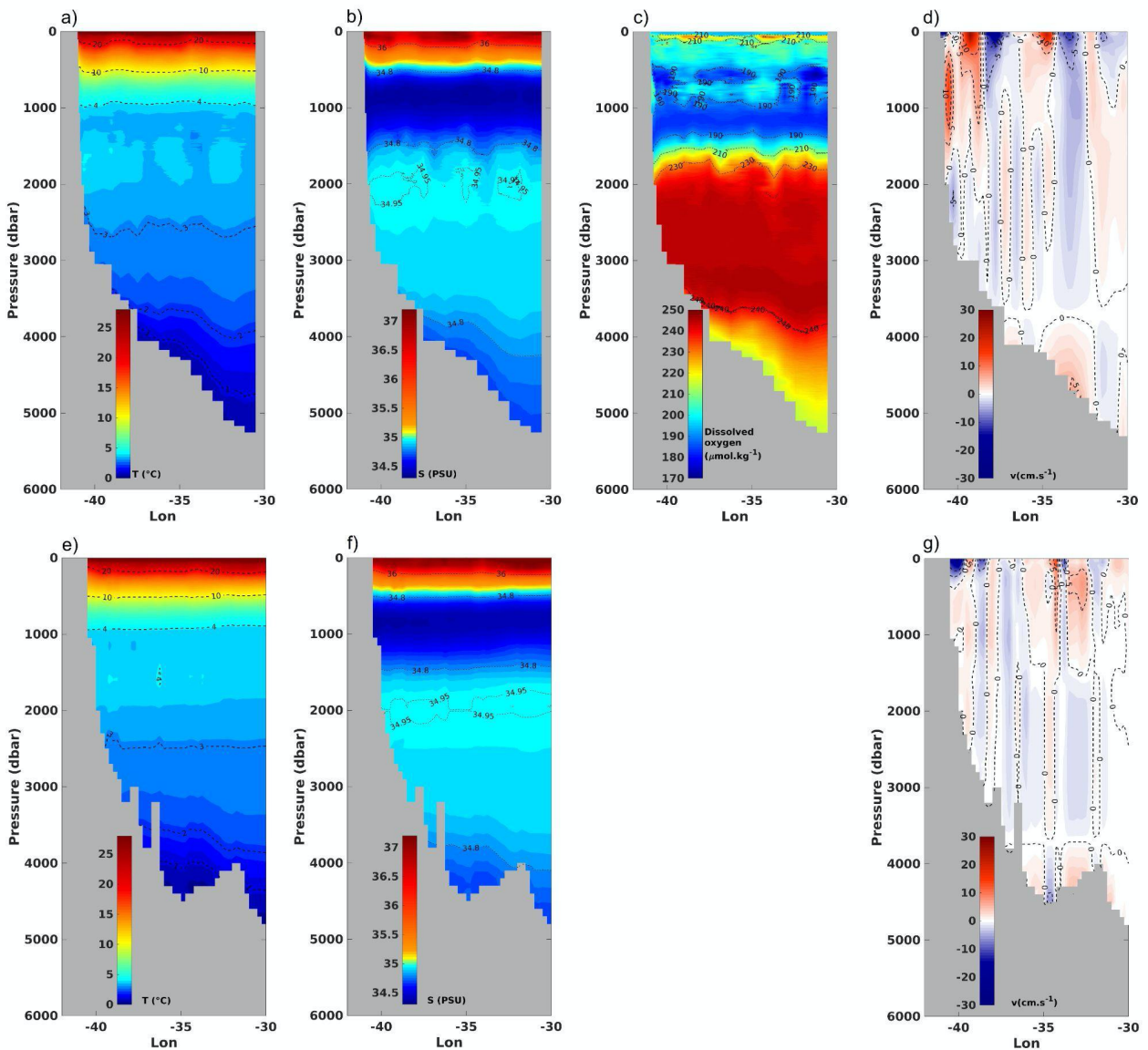
370 This subsection covers the water masses captured by the AXMOC data and compares its
 371 results with alternative independent in situ data from WOCE. The transbasin section at 22.5°S is
 372 characterized by more intense circulation on both boundaries in comparison to the interior of the
 373 section (Figure 7). Most of the variability along the section is concentrated in the upper ocean
 374 and near the boundaries (Figure 7b).



375

376 **Figure 7.** Mean northward velocity (a) and its standard deviation (b) computed from the
 377 AXMOC data. Main water masses (a) and ocean currents (b) are indicated: Tropical Water
 378 (TW), South Atlantic Central Water (SACW), Antarctic Intermediate Water (AAIW), North
 379 Atlantic Deep Water (NADW), Antarctic Bottom Water (AABW), Brazil Current (BC),
 380 Benguela Current (BeC), Intermediate Western Boundary Current (IWBC), Deep Western
 381 Boundary Current (DWBC) and Deep Eastern Boundary Current (DEBC). Neutral density
 382 isopycnals are represented by dashed lines (a). Solid lines indicate contour of no meridional
 383 velocity (b).

384 The AABW is the deep equatorward flow (>4000 m) confined in the western boundary
 385 west of 30°W, constrained by the Trindade Island topography, and its mean flow reaches speeds
 386 of $0.02 \pm 0.01 \text{ m s}^{-1}$ at 22.5°S (Figure 7). The AABW is characterized by $T < 2^\circ\text{C}$, $S < 34.8$ and
 387 reduced dissolved oxygen levels ($\text{O}_2 \approx 220 \mu\text{mol kg}^{-1}$) relative to NADW (Figures 8 and S1),
 388 which is in agreement with Reid et al. (1989). Between 50°S and the equator, the AABW flows
 389 along neutral density lines $\gamma > 28.10 \text{ kg m}^{-3}$ (Liu & Tanhua, 20219).



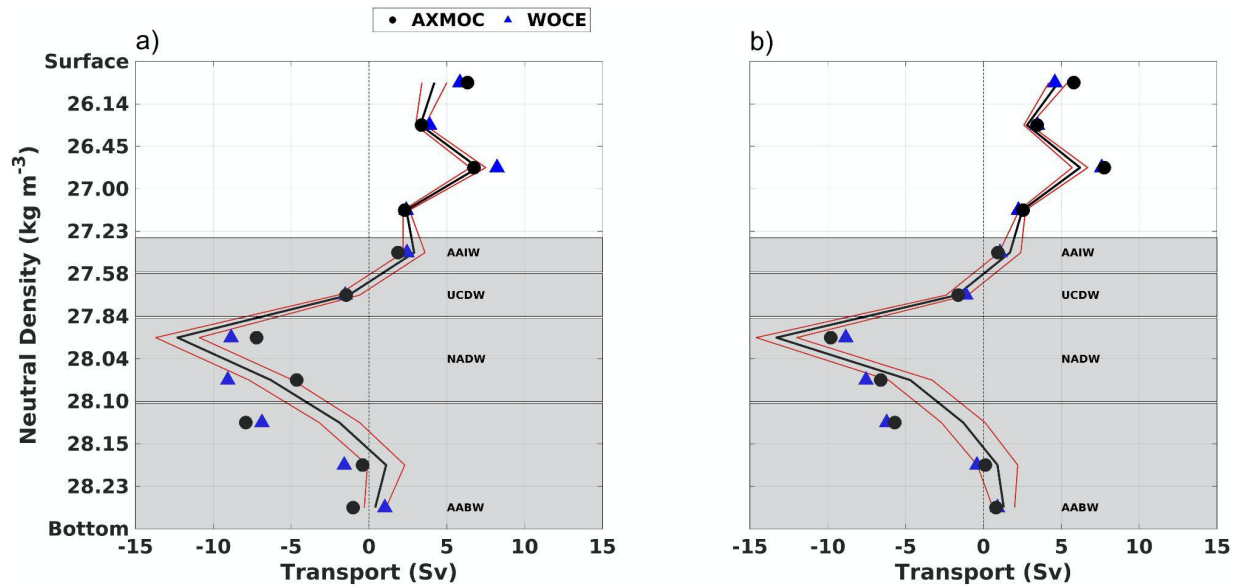
391 **Figure 8.** Ocean tracers and velocity section focused on western boundary for April 2009 at 24
 392 and 22.5°S. A-d (e-g) panels represent WOCE (AXMOC) dataset. Temperature (T), salinity (S),
 393 dissolved oxygen and velocity (v) are shown between western boundary and 30°W.

394 Similar to the AABW, the NADW is also confined by local topography near the western
 395 boundary. Near the eastern boundary (Figure 7), a secondary southward NADW branch is also
 396 visible. Indeed, the NADW has been reported to split into two branches before crossing 22°S:
 397 one branch remains flowing southward near the western boundary and another branch flows
 398 eastward along the equator (Talley, 2011). Both branches are located between 1700 and 3600 m
 399 and the western branch is more intense, reaching up to $-0.01 \pm 0.01 \text{ m s}^{-1}$ at 22.5°S (Figure 7).
 400 In the tropics, the NADW is usually divided vertically into the upper (uNADW) and lower
 401 NADW (INADW - Talley 2011) cores. As it flows southward, vertical mixing slowly merges
 402 this two-lobed water mass into one main core flowing between neutral density surfaces of 27.84
 403 and 28.10 kg m^{-3} (e.g., Hernandez-Guerra et al., 2019; Liu & Tanhua, 2021; Stramma et al.,
 404 2004). This single core signal is observed on both branches of the NADW (Figure 7), which is
 405 characterized by a local maximum in salinity ($S > 34.85$) and a maximum in dissolved oxygen
 406 ($\text{O}_2 > 240 \mu\text{mol kg}^{-1}$) near the western boundary (Figure 8).

407 The Upper Circumpolar Deep Water (UCDW) is defined as a fresh (core S around 34.6),
 408 low oxygen water mass with neutral density between 27.58 and 27.84 kg m^{-3} and located
 409 between 1150 and 1550 m deep (e.g., Hernandez-Guerra et al., 2019). It is characterized by low
 410 salinity ($S < 34.8$) and poor oxygen levels ($\text{O}_2 < 190 \mu\text{mol kg}^{-1}$; Figure 8). Located above the
 411 UCDW, at depths varying from 700 and 1150 m, the Antarctic Intermediate Water (AAIW) is
 412 characterized by a minimum salinity at its core ($S < 34.5$) located around 800 m, and relatively
 413 high oxygen levels, flowing along neutral densities between 27.23 and 27.58 kg m^{-3} . Both
 414 UCDW and AAIW form the Intermediate Western Boundary Current system (IWBC) at 22.5°S
 415 (Figure 7), which is characterized by an equatorward flow near 38°W between about 600 and
 416 1700 m depth (Figure 7).

417 The isolines of T, S and dissolved oxygen in the AXMOC and WOCE data are located at
 418 similar depths (Figure 8 and S1). The isolines of the WOCE data are more variable, while the
 419 AXMOC isolines are smoother because of the time and space averaging applied during the
 420 mapping procedure. The WOCE data is based on CTD casts, and has not been smoothed.

421 A direct comparison of volume transport per neutral density intervals is an important step
 422 to evaluate the mapping methodology applied here (Figure 9). While AXMOC and WOCE
 423 estimations are calculated from their respective T-S profiles, Cainzos et al. (2022) employ an
 424 inverse box model to compute decadal AMOC estimates from WOCE transects. The top layer
 425 (from surface to $\sigma = 26.45 \text{ kg m}^{-3}$) is composed by the geostrophic transport and the Ekman
 426 transport, while the remaining intervals are composed solely by the geostrophic transport. A
 427 good agreement exists between AXMOC and WOCE volume transport estimates in the upper
 428 1000 m, characterized by $\sigma < 27.58 \text{ kg m}^{-3}$. The AXMOC data show a transport of 20.60 Sv and
 429 20.48 Sv for Apr/2009 and Mar/2018, respectively. The volume transports in the WOCE data are
 430 22.78 Sv and 18.95 Sv for Apr/2009 and Mar/2018, respectively. The difference between the
 431 WOCE and the AXMOC data in the upper ocean ($\sigma < 27.58 \text{ kg m}^{-3}$) is generally within the
 432 uncertainty interval estimated by Cainzos et al. (2022).



433

434 **Figure 9.** Volume transport at different neutral density levels for two different months: Apr/2009
 435 (left panel) and Mar/2018 (right panel). AXMOC data is represented by black circles and WOCE
 436 data by blue triangles. Black line and red lines represent the volume transport and its
 437 uncertainties estimated by the inverse model of Cainzos et al. (2022) for the decades of (left)
 438 2000s and (right) 2010s decades. The gray areas represent the density ranges of the main water
 439 masses across the section: Antarctic Intermediate Water (AAIW), Upper Circumpolar Deep
 440 Water (uCDW), North Atlantic Deep Water (NADW) and Antarctic Bottom Water (AABW).

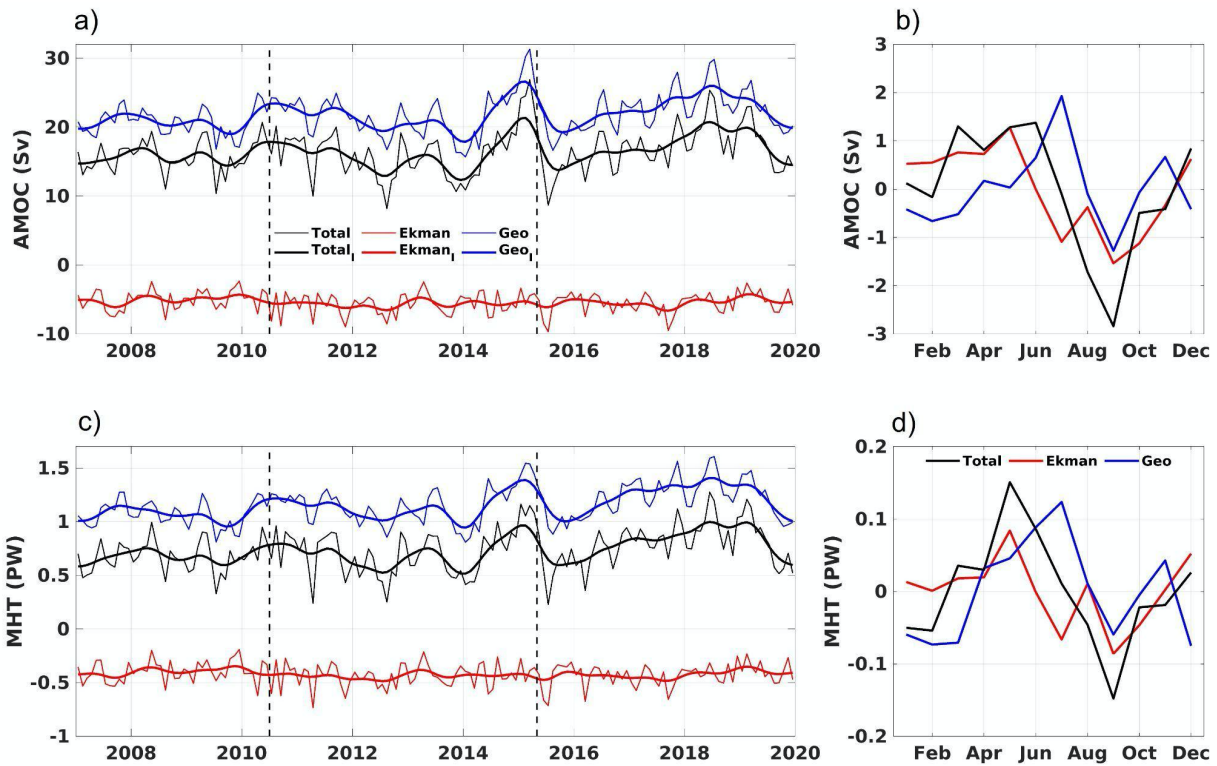
441 The area encompassing upper layer boundary currents ($\gamma < 27.23 \text{ kg m}^{-3}$), i.e., BC and
 442 BeC, has a positive net volume transport of 18.74 Sv and 19.55 Sv for Apr/2009 and Mar/2018,
 443 respectively (Figure 9). For WOCE data, the volume transports are 20.34 Sv and 17.89 Sv for
 444 Apr/2009 and Mar/2018, respectively. AXMOC and WOCE results are similar in every level for
 445 both periods analyzed (Apr/2009 and Mar/2018), and this similarity is also observed with the
 446 decadal results from Cainzos et al. (2022). At 22.5°S , the upper AMOC cell is located from
 447 surface to $\gamma=27.58 \text{ kg m}^{-3}$, and the lower AMOC cell is located from $\gamma=27.58 \text{ kg m}^{-3}$ to the
 448 bottom. Considering the layer encompassing the UCDW, the resulting AXMOC-based transport
 449 is slightly negative of -1.47 Sv and -1.62 Sv for Apr/2009 and Mar/2018, respectively (Figure
 450 9), because the more intense intermediate equatorward currents are limited to the western
 451 boundary, while the interior and eastern boundary have poleward flow (Figure 7). In both periods
 452 analyzed, the NADW is the main conduit of the lower AMOC cell from neutral density of 27.84
 453 to 28.10 kg m^{-3} (Figure 9). Finally, the resulting transport on the layer encompassing the
 454 AABW turns back poleward mainly because of the influence of the deep western boundary
 455 current. The mapping methodology is robust considering that most of its estimates fall within 2
 456 times the uncertainty levels of the independent study performed by Cainzos et al. (2022),
 457 especially in the upper ocean. It is important to highlight that both sections, AXMOC and
 458 WOCE (also used as reference in Cainzos et al., 2022), are not located at the same latitude.
 459 WOCE section is located around 24°S and AXMOC transect location varies between 20.5 and
 460 23°S . Greater differences from AXMOC, WOCE and Cainzos et al. (2022) are observed in areas
 461 with $\gamma > 27.84 \text{ kg m}^{-3}$, because of uncertainties inherent in the methodology and use of
 462 WOA18 climatology data on the AXMOC section in areas without XB and Argo observations.

463 3.4 AMOC and MHT time series

464 In this subsection, the newly produced AMOC and MHT time series from AXMOC data
 465 are presented along with their contributions from geostrophic and Ekman components. The
 466 correlations of AMOC and MHT with each component and with estimates from other datasets
 467 are also discussed and presented in the supplementary material (Figures S2-S4). Finally, the
 468 influence of western and eastern boundaries, and the interior region of the ocean is addressed.

469 3.4.1 Mean and Seasonal cycle

470 The estimated mean AMOC (MHT) transport from AXMOC data is 16.34 ± 3.20 Sv
 471 (0.73 ± 0.20 PW) between 2007 and 2020. The total AMOC (MHT) transport from AXMOC is
 472 composed by an intense equatorward geostrophic transport of 21.74 ± 2.85 Sv (1.15 ± 0.17 PW)
 473 and a significant poleward AMOC (MHT) Ekman component of -5.41 ± 1.49 Sv (-0.43 ± 0.11 PW)
 474 - Figure 10 and Table 1). On a seasonal time scale, the AMOC is stronger in June and weaker in
 475 September, and the MHT is more intense in May and weaker in September (Figure 10).



476
 477 **Figure 10.** AMOC and MHT time series (left) and associated seasonal cycles (right). AMOC (a,
 478 c) and MHT (d, f) time series are divided into Geostrophic (blue lines), Ekman (red lines) and
 479 total components (black lines). Solid lines represent the 13-month gaussian filtered component of
 480 AMOC and MHT (a and c, respectively). Vertical black dashed lines indicate dates of 06/2010
 481 and 04/2015.

482

	Total	Geostrophic	Ekman
--	-------	-------------	-------

	AMOC	MHT	AMOC	MHT	AMOC	MHT
AXMOC	16.34±3.20	0.72±0.20	21.74±2.85	1.15±0.17	-5.41±1.49	-0.42±0.10
Dong - 20°S	16.45±2.13	0.62±0.17	22.70±1.49	1.20±0.09	-6.26±1.66	-0.58±0.14
Dong - 25°S	19.30±2.20	0.68±0.17	23.00±1.64	1.01±0.12	-3.70±1.42	-0.33±0.13
ECCOv4r4	14.11±2.55	0.48±0.16	19.13±1.84	0.87±0.10	-5.01±1.38	-0.39±0.10

483 **Table 1.** Mean and std values for AMOC (Sv) and MHT (PW) between 2007 and 2019. Total,
484 geostrophic and Ekman components are represented in separated columns.

485 A comparison of the AMOC (MHT) from AXMOC with that from Dong et al. (2021)
486 synthetic product and the ECCOv4r4 state estimate is shown in the Supplementary Material
487 (Figures S2-S4). The seasonal variations in the AMOC and MHT also have similar patterns to
488 other products which present positive values from April until July and negative values between
489 August and October (Figure S3). Overall, the mean values from AXMOC are within the
490 uncertainty ranges of the other products for both AMOC and MHT (Table 1 and Figure S2).
491 Correlations between AXMOC and individual products are higher for the MHT than for the
492 AMOC: $r=0.40$ (Dong et al., 2021 - 20°S), $r=0.35$ (Dong et al., 2021 - 25°S), and $r=0.29$
493 (ECCOv4r4) for the AMOC and $r=0.59$ (Dong et al., 2021 - 20°S), $r=0.51$ (Dong et al., 2021 -
494 25°S) and $r=0.44$ (ECCOv4r4) for the MHT. This relatively low correlation between the
495 AXMOC and the other datasets can be related to the amount of variance explained by the
496 geostrophic component of the AMOC/MHT. The variance explained by the geostrophic and
497 Ekman components of the AMOC are similar in Dong et al. (2021) and in the ECCOv4r4 data,
498 approximately 40-60% for each component (Table 2). For the AXMOC, however, the
499 geostrophic component is responsible for most (83%) of the total transport variance. The
500 geostrophic component can also explain the stronger variability of the AMOC/MHT in the
501 AXMOC time series (Table 1).

	AXMOC	Dong - 20°S	Dong - 25°S	ECCOv4r4
Geostrophic	0.83 (0.77)	0.41 (0.33)	0.60 (0.44)	0.51 (0.58)
Ekman	0.17 (0.23)	0.59 (0.67)	0.40 (0.56)	0.49 (0.42)

502 **Table 2.** AMOC variance explained by its geostrophic/Ekman components. The MHT variance
503 explained by its geostrophic/Ekman components are presented in parenthesis.

504 3.4.2 Interannual variability

505 The low-pass filtered geostrophic component shows a strong correlation with the total
506 component for both AMOC and MHT ($r=0.96$ and $r=0.97$, respectively), thus most of the AMOC
507 and MHT variability in the interannual band is explained by the geostrophic transport (Figure
508 10). The AMOC decreases significantly when there are intense BC events (Figure 4), as
509 observed during years 2011, 2014, 2015 and 2019. Previous studies indicate that the dominance
510 of geostrophic and Ekman components on the AMOC varies at different latitudes in the South
511 Atlantic. At 35°S, the relative dominance of Ekman and geostrophic components on AMOC and

512 MHT alternates throughout the time (Dong et al., 2015, 2021). Ekman dominance is also
 513 observed at 20°S, but a greater contribution of the geostrophic component is reported at 25°S
 514 (Dong et al., 2015). Results from the AXMOC transect corroborate with Dong et al. (2015, 2021)
 515 25°S estimates on the overall dominance of the geostrophic component (correlations of
 516 0.94/0.92) over the Ekman contribution (correlations of 0.15/0.21) for AMOC/MHT transports.
 517 In addition, high correlations ($r > 0.95$) are observed between the total AMOC and MHT time
 518 series at 22.5°S, as well as for the geostrophic and Ekman components. Other studies have also
 519 observed high correlations between the AMOC and MHT time series at various latitudes in both
 520 the North and South Atlantic (Dong et al., 2009, 2015, 2021; Johns et al., 2011), showing the
 521 dominance of velocity variability over temperature variability in the MHT time series.

522 The variability observed in the AXMOC time series appears to have changed since 2014,
 523 when the interannual to decadal variability strengthened, driving an increase in the AMOC by
 524 approximately 2 Sv (Figure 10). Dong et al. (2021) also observed a moderate interannual AMOC
 525 increase at 25°S on both total and geostrophic transports but only after 2017 (Figure S4). Due to
 526 the short extent of our time series we cannot draw any conclusion about the long term changes of
 527 the AMOC. Next, we will compare AXMOC time series with the decadal estimates of Cainzos et
 528 al. (2022), Dong et al. (2021) and ECCOV4r4, analyze it in the context of decadal variability.

529 3.4.3 Decadal variability

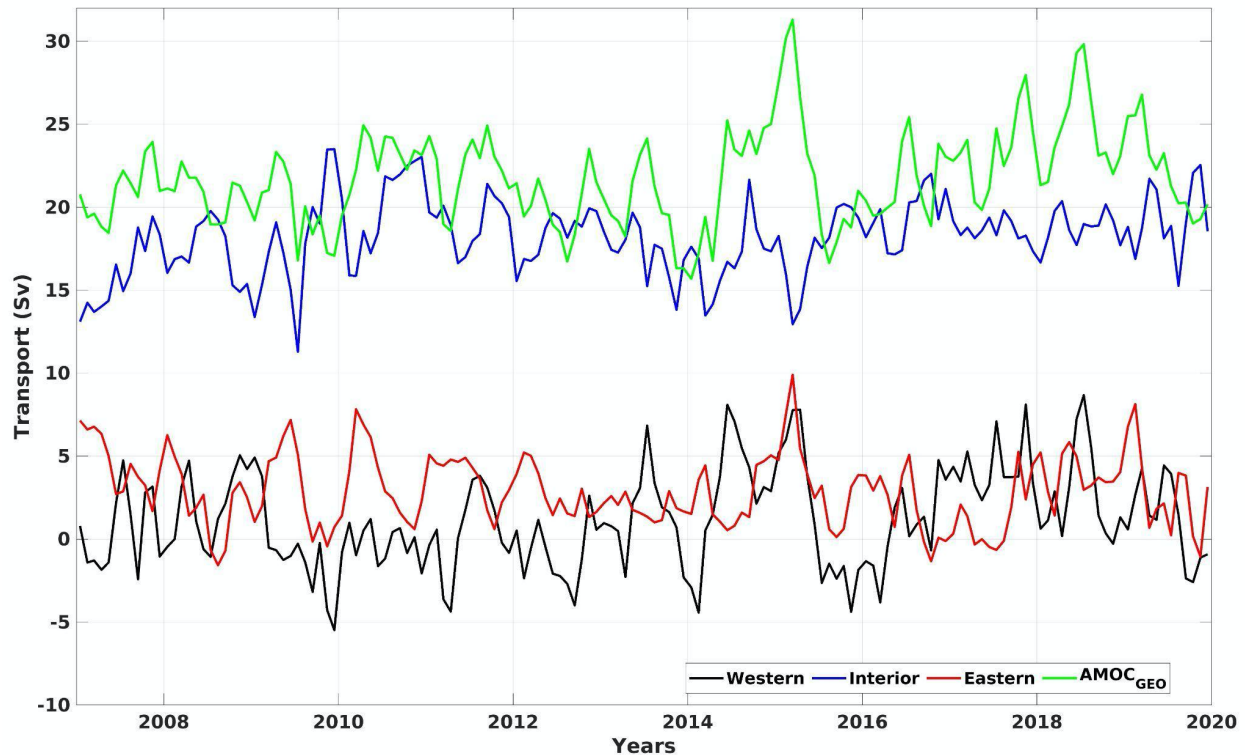
530 We estimated the AMOC transport using the WOCE/GO-SHIP data applying the same
 531 methodology used in the AXMOC. For the two WOCE sections of Apr/2009 and Mar/2018, the
 532 AMOC strength was 22.00 Sv and 18.59 Sv, respectively. The corresponding AMOC transports
 533 from the AXMOC data are 24.8 Sv and 19.96 Sv. The AXMOC estimates differ from WOCE
 534 estimates by +2.80 Sv and -0.63 Sv, respectively. Therefore, we estimate the error due to spatial
 535 mapping and data availability to be of ~ 2 Sv. To compare the decadal variability of AXMOC
 536 and other products, we used the 2010-2019 mean AMOC. The AXMOC mean of 2010-2019
 537 AMOC value is 16.58 ± 3.41 Sv, in comparison to 16.29 ± 2.14 Sv (20°S) and 19.26 ± 2.30 Sv
 538 (25°S) for Dong et al. (2021) and significantly smaller value for ECCOV4r4 of 13.75 ± 2.39 Sv.
 539 Relative to the previous decade, Dong et al. (2021) observed contrasting changes such as a slight
 540 increase (0.19 Sv) in 25°S and a slight decrease (-0.58 Sv) in 20°S, while ECCOV4r4 showed an
 541 AMOC decrease of 1.19 Sv between the two periods.

542 Results from the Cainzos et al. (2022) adjoint model show a mean AMOC decrease of \sim
 543 1.6 Sv from 2000-2009 to 2010-2019, 19.70 ± 1.20 Sv to 18.10 ± 1.10 Sv, respectively, which falls
 544 within the uncertainties of the methodology applied. The difference from Cainzos et al. (2022)
 545 and the AXMOC decadal means is also within 2 Sv. In addition, Cainzos et al. (2022) estimated
 546 a slightly higher mean AMOC of 19.80 ± 1.00 Sv for the 1990-1999 decade. Therefore, our results
 547 corroborate to the conclusions drawn by Cainzos et al. (2022) that no significant changes were
 548 observed in the AMOC near 22.5S in the past three decades.

549 3.4.4 Boundary and Interior contributions

550 Finally, to understand if the specific areas of the AXMOC transect influence the AMOC
 551 at 22.5°S, we compare its geostrophic component to the transport in the upper 1000 m near the
 552 western boundary (from western coast to 38°W), interior of the section (from 39°W to 3°E), and
 553 near the eastern boundary (from 3°E to eastern coast). The AMOC geostrophic transport has a
 554 higher correlation with the western ($r=0.69$) than with the eastern boundary ($r=0.41$) (Figure 11).

555 This is different to what was observed at 34.5°S, where the eastern boundary contributes more to
 556 the AMOC variability than the western boundary (Meinen et al., 2018). A possible explanation
 557 for this difference is the increased influence of the Agulhas leakage in the eastern boundary close
 558 to 34.5°S. In addition, the interior and eastern boundary transports show a significant inverse
 559 relationship ($r = -0.62$) and compensation between the two regions (Figure 10). The anomalous
 560 strengthening of the AMOC in 2015 (Figure 10a), where the geostrophic contribution reached
 561 values close to 25 Sv, is due to a concurrent intensification of equatorward circulation on both
 562 boundaries (Figure 11). Apart from that, most of the AMOC anomalous intensification events are
 563 caused by the changes in only one of the boundaries.



564

565 **Figure 11.** Upper 1000 m volume transport for western boundary (black), eastern boundary (red)
 566 and interior (blue) from the AXMOC data. The geostrophic AMOC transport is shown by a
 567 green line.

568 4 Conclusions

569 We use a combination of Argo and XBT data to produce the first estimate of the AMOC
 570 and MHT at 22.5°S. The current in situ coverage composed by Argo and XBT data is sufficient
 571 for the calculation of AMOC and MHT at 22.5°S from 2007 onwards. The altimetry optimized
 572 mapping methodology proved to be efficient in capturing westward wave propagation, boundary
 573 currents, AMOC and MHT. Near the western boundary, the first continuous long-term monthly
 574 transport of the highly variable BC was produced due to the good coverage by the high-density
 575 XBT transect implemented since 2004. BC volume transport anomalies observed in 2009/2010
 576 are consistent with Goes et al. (2019). These and other BC anomalies (e.g., 2014 and 2016) are
 577 captured by AXMOC data and observed in the SLA time series at the western boundary.

578 Some physical properties (T , S and γ) of the main water masses in the South Atlantic
579 were also analyzed here, and are consistent with earlier studies (Hernandez-Guerra et al., 2019;
580 Liu & Tanhua, 2021; Stramma et al., 2004 and Talley, 2011). The AABW is limited by neutral
581 density lines $\gamma > 28.10 \text{ kg m}^{-3}$, while the NADW flows between 27.84 and 28.10 kg m^{-3} . At
582 22.5°S, both AABW and NADW are constrained west of 30°W by local topography and the
583 latter is divided into two cores flowing along the western and eastern boundaries near depths of
584 2500 m. In the uppermost isopycnal layer ($\gamma < 27.23 \text{ kg m}^{-3}$), an important area for AMOC
585 variability, AXMOC and WOCE data have a good agreement. The AXMOC data yields volume
586 transports of 18.74 Sv and 19.55 Sv for Apr/2009 and Mar/2018, respectively, while WOCE data
587 yields volume transports of 20.34 Sv and 17.89 Sv for the same period, respectively. The
588 integrated isopycnal transport obtained by AXMOC is robust and an uncertainty of ~ 2 Sv in the
589 AMOC transport due to the mapping errors is estimated from independent observations.

590 Seasonality in the AMOC and MHT time series shows a good agreement between all the
591 products considered, with annual amplitudes of 4 Sv and 0.3 PW, respectively. Stronger
592 AMOC/MHT values are observed in Jan-Jul and weaker values are observed in Aug-Dec. The
593 geostrophic and Ekman contributions are in-phase and reinforce this variability. The interannual
594 variability in the geostrophic component of the AMOC from AXMOC is more intense than those
595 from other products, probably because of the improved resolution near the western boundary.
596 The western boundary currents appear to have the largest contribution to the AMOC/MHT
597 variability ($r=0.62$). Our results show sharp declines in the AMOC and MHT during positive BC
598 anomalies (intense southward transport), such as in 2014, end of 2015 and 2019. Also, a period
599 of more frequent negative values of total and geostrophic transports in both AMOC and MHT is
600 observed between 2010 and 2015. Further analysis is needed, but the basin wide extent of this
601 event suggests that they are related to large scale modes of variability in the South Atlantic.
602 Finally, AXMOC data could also be used to assess freshwater flux anomalies in the South
603 Atlantic and link it to a possible bi-stability of the AMOC (Rahmstorf et al., 1996; Stommel,
604 1961).

605 The observed AMOC (MHT) mean transport was 16.34 ± 3.20 Sv (0.73 ± 0.20 PW)
606 between 2007 and 2020, and positive anomalies became more frequent after 2015 (Figures 10
607 and S4), although this trend was not statistically significant given the uncertainty of our
608 estimates. The AMOC is projected to weaken according to the IPCC projections for the 21st
609 century (Collins et al., 2019; Fox-Kemper et al., 2021; Lee et al., 2021). The future AMOC
610 weakening has been linked to a BC intensification (Marcello et al., 2023), and our results
611 corroborate with this link between the BC and the AMOC at 22.5°S, thus the continuation of this
612 monitoring effort at 22.5°S might provide early evidence for changes in the AMOC in the
613 Northern Hemisphere.

614 The availability of multi-decadal data of tide gauges on both sides of the basin can in the
615 future be used to complement, validate, and extend the DH field on the boundaries. Deep Argo
616 profilers and/or PIES stations have the potential to improve data availability in the South Atlantic
617 deep ocean (>2000 m), and could replace climatological data in the deep ocean, since their
618 spatial and temporal coverage has been increasing significantly. The proposed methodology can
619 be replicated to include other latitudes in the Atlantic basin where the Argo and XBT coverage
620 would permit a long term AMOC and MHT estimations. This expansion to other latitudes would
621 be beneficial for the scientific community once an integrated assessment of the long-term
622 variability of AMOC and MHT can be performed using a single methodology. Currently, the

623 AMOC has been monitored at different latitudes, however, each program has different
624 limitations and uncertainties, which impacts the comparison and integration of different time
625 series (Chidichimo et al., 2023). In addition, our methodology allows more frequent updates of
626 the AMOC since Argo and XBT data are publicly available in near-real time, as opposed to
627 mooring data from existing AMOC arrays. Therefore, our methodology, if expanded in time and
628 space, could positively impact the prediction capability of different events (e.g., coastal sea level
629 and hurricane season outlook).

630 **Acknowledgments**

631 This research was carried out in part under the auspices of the Cooperative Institute for
632 Marine and Atmospheric Studies, a cooperative institute of the University of Miami and the
633 National Oceanic and Atmospheric Administration (NOAA), cooperative agreement NA
634 20OAR4320472, and was supported by the Ocean Observing and Monitoring Division of the
635 NOAA Climate Program Office and by NOAA's Atlantic Oceanographic and Meteorological
636 Laboratory (AOML). MG and DLV were also supported by the National Oceanic and
637 Atmospheric Administration (NOAA) Climate Variability and Predictability program (grant
638 number NA20OAR4310407).

640 **Open Research**

641 The following data used for this study can be downloaded from: XBT transect data
642 (<http://www.aoml.noaa.gov/phod/hdenxbt/>); Argo profile data (<https://www.nodc.noaa.gov/argo/> and
643 <https://www.seanoe.org/data/00311/42182/> - <http://doi.org/10.17882/42182>); Argo/altimetry
644 climatological ADT product (<http://apdrc.soest.hawaii.edu/projects/argo/>); the delayed-time satellite
645 altimetry maps (<http://marine.copernicus.eu>); ERA5 atmospheric reanalysis
646 (<https://cds.climate.copernicus.eu>); MOC and MHT synthetic time series
647 (https://www.aoml.noaa.gov/phod/samoc_argo_altimetry/data_moc.php); WOA18
648 (<https://www.ncei.noaa.gov/access/world-ocean-atlas-2018/>); RG Argo ([https://sio-
649 argo.ucsd.edu/RG_Climatology.htm](https://sio-argo.ucsd.edu/RG_Climatology.htm)); ECCOv4r4 ([https://www.ecco-group.org/products-ECCO-
651 V4r4.html](https://www.ecco-group.org/products-ECCO-
650 V4r4.html)); WOCE (<https://cchdo.ucsd.edu>) for cruises A095 in 2009
652 (<https://cchdo.ucsd.edu/cruise/740H20090307>) and in 2018
653 (<https://cchdo.ucsd.edu/cruise/740H20180228>).

653

654

655

656 **References**

657 Ablain, M., Meyssignac, B., Zawadzki, L., Jugier, R., Ribes, A., Spada, G., et al. (2019).

658 Uncertainty in satellite estimates of global mean sea-level changes, trend and acceleration. *Earth*

659 *Syst. Sci. Data*, 11, 1189–1202. doi:10.5194/essd-11-1189-2019.

660

661 Argo (2020). Argo float data and metadata from Global Data Assembly Centre (Argo GDAC).

662 SEANOE. doi:10.17882/42182

663

664 Arnault, S., Gourdeau, L., & Menard, Y. (1992). Comparison of the altimetric signal with in situ

665 measurements in the tropical Atlantic Ocean. *Deep Sea Research Part A. Oceanographic*

666 *Research Papers*, 39(3-4), 481-499. doi:10.1016/0198-0149(92)90084-7

667

668 Barron, C. N., Kara, A. B., & Jacobs, G. A. (2009). Objective estimates of westward Rossby

669 wave and eddy propagation from sea surface height analyses. *Journal of Geophysical Research*

670 *Oceans*, 114(C3), 496-510. doi:10.1029/2008JC005044

671

672 Bellomo, K., Angeloni, M., Corti, S., & von Hardenberg, J. (2021). Future climate change

673 shaped by inter-model differences in Atlantic meridional overturning circulation response.

674 *Nature Communications*, 12(1), 1-10. doi:10.1038/s41467-021-24015-w

675

676 Berger, W. H., Wefer, G., Richter, C., Lange, C. B., Giraudeau, J., Hermelin, O., & Party, S. S.

677 (1998). 17. The Angola-Benguela upwelling system: Paleoceanographic synthesis of shipboard

678 results from leg 1751. In Proceedings Ocean Drilling Program, Initial Reports (Vol. 175, pp.
679 505-531). doi:10.2973/odp.proc.ir.175.117.1998

680

681 Biastoch, A., Böning, C. W., Schwarzkopf, F. U. & Lutjeharms, J. R. E. (2009), Increase in
682 Agulhas leakage due to poleward shift of Southern Hemisphere westerlies, *Nature*, 462(7272),
683 495-498. doi:10.1038/nature08519.

684

685 Broecker, W. S. (2003). Does the trigger for abrupt climate change reside in the ocean or in the
686 atmosphere? *Science*, 300(5625), 1519-1522. doi:10.1126/science.1083797

687

688 Buckley, M. W., & Marshall, J. (2016). Observations, inferences, and mechanisms of the
689 Atlantic Meridional Overturning Circulation: A review. *Reviews of Geophysics*, 54(1), 5-63.
690 doi:10.1002/2015RG000493

691

692 Caínzos, V., Hernández-Guerra, A., McCarthy, G. D., McDonagh, E. L., Cubas Armas, M., &
693 Pérez-Hernández, M. D. (2022). Thirty years of GOSHIP and WOCE data: Atlantic overturning
694 of mass, heat, and freshwater transport. *Geophysical Research Letters*, 49(4), e2021GL096527.

695 doi:10.1029/2021GL096527

696

697 Calado, L., Gangopadhyay, A., & Da Silveira, I. C. A. (2008). Feature-oriented regional
698 modeling and simulations (FORMS) for the western South Atlantic: Southeastern Brazil region.

699 *Ocean Modelling*, 25(1-2), 48-64. doi:10.1016/j.ocemod.2008.06.007

700

701 Chang, P., Zhang, R., Hazeleger, W., Wen, C., Wan, X., Ji, L., et al. (2008), Oceanic link
702 between abrupt changes in the North Atlantic Ocean and the African monsoon, *Nature*
703 *Geoscience*, 1(7), 444-448. doi:10.1038/ngeo218.
704

705 Chidichimo, M.P., Perez, R.C., Speich, S., Kersalé, M., Sprintall, J., Dong, S., et al. (2023),
706 Energetic overturning flows, dynamic interocean exchanges, and ocean warming observed in the
707 South Atlantic. *Communications Earth Environment* 4, 10. doi:1038/s43247-022-00644-x
708

709 Collins, M., Sutherland, M., Bouwer L., Cheong, S. M., Frölicher, T., Jacot Des Combes, H., et
710 al. (2019). *Extremes, Abrupt Changes and Managing Risk*. In Pörtner H. O., Roberts, D. C.,
711 Masson-Delmotte, V., Zhai, P., Tignor, M., Poloczanska, E., et al. (eds.), *IPCC Special Report*
712 *on the Ocean and Cryosphere in a Changing Climate*. Cambridge University Press, Cambridge,
713 UK and New York, NY, pp. 589-655. doi:10.1017/9781009157964.008.
714

715 Conway, T. M., Palter, J. B., & de Souza, G. F. (2018). Gulf Stream rings as a source of iron to
716 the North Atlantic subtropical gyre. *Nature Geoscience*, 11(8), 594-598. doi:10.1038/s41561-
717 018-0162-0
718

719 Da Silveira, I. C. A., Lima, J. A. M., Schmidt, A. C. K., Ceccopieri, W., Sartori, A., Francisco,
720 C. P. F., & Fontes, R. F. C. (2008). Is the meander growth in the Brazil Current system off
721 Southeast Brazil due to baroclinic instability? *Dynamics of Atmospheres and Oceans*, 45(3-4),
722 187-207. doi:10.1016/j.dynatmoce.2008.01.002
723

724 Desbruyères, D., Chafik, L. & Maze, G. (2021). A shift in the ocean circulation has warmed the
725 subpolar North Atlantic Ocean since 2016. *Commun Earth Environ* 2, 48. doi:/10.1038/s43247-
726 021-00120-y.

727

728 de Vries, P., & Weber, S. L. (2005). The Atlantic freshwater budget as a diagnostic for the
729 existence of a stable shut down of the meridional overturning circulation. *Geophysical Research*
730 *Letters*, 32(9), L09606. doi:10.1029/2004GL021450

731

732 Dong, S., Garzoli, S., Baringer, M., Meinen, C., & Goni, G. (2009). Interannual variations in the
733 Atlantic meridional overturning circulation and its relationship with the net northward heat
734 transport in the South Atlantic. *Geophysical Research Letters*, 36(20). doi:

735 10.1029/2009GL039356

736

737 Dong, S., Goni, G., & Bringas, F. (2015). Temporal variability of the South Atlantic meridional
738 overturning circulation between 20 S and 35 S. *Geophysical Research Letters*, 42(18), 7655-
739 7662. doi:10.1002/2015GL065603

740

741 Dong, S., Goni, G., Domingues, R., Bringas, F., Goes, M., Christophersen, J., & Baringer, M.
742 (2021). Synergy of in situ and satellite ocean observations in determining meridional heat

743 transport in the Atlantic Ocean. *Journal of Geophysical Research: Oceans*, 126(4). doi:

744 10.1029/2020JC017073

745

746 Durgadoo, J. V., Loveday, B. R., Reason, C. J., Penven, P. & Biastoch, A. (2013), Agulhas
747 leakage predominantly responds to the Southern Hemisphere westerlies, *Journal of Physical*
748 *Oceanography*, 43(10), 2113-2131. doi:10.1175/JPO-D-13-047.1.
749

750 Forget, G., Campin, J.-M., Heimbach, P., Hill, C. N., Ponte, R. M. & Wunsch, C. (2015). ECCO
751 version 4: An integrated framework for non-linear inverse modeling and global ocean state
752 estimation. *Geoscientific Model Development*, 8. 3071-3104. doi:10.5194/gmd-8-3071-2015
753

754 Fox-Kemper, B., Hewitt, H.T., Xiao, C., Aðalgeirsdóttir, G., Drijfhout, S.S., Edwards, T.L., et al.
755 (2021). Ocean, Cryosphere and Sea Level Change. In Masson-Delmotte, V., P. Zhai, A. Pirani,
756 S.L. Connors, C. Péan, S. Berger, et al. (eds.), *Climate Change 2021: The Physical Science*
757 *Basis. Contribution of Working Group I to the Sixth Assessment Report of the*
758 *Intergovernmental Panel on Climate Change*. Cambridge University Press, Cambridge, United
759 Kingdom and New York, NY, USA, pp. 1211–1362. doi:10.1017/9781009157896.011
760

761 Frajka-Williams, E., Anson, I. J., Baehr, J., Bryden, H. L., Chidichimo, M. P., Cunningham, S.
762 A., et al. (2019), Atlantic Meridional Overturning Circulation: Observed Transport and
763 Variability, *Frontiers in Marine Science*, 6(260). doi:10.3389/fmars.2019.00260.
764

765 Garcia H.E., Boyer, T.P., Baranova, O.K., Locarnini, R.A., Mishonov, A.V., Grodsky, A., et al.
766 (2019). *World Ocean Atlas 2018: Product Documentation*. A. Mishonov, Technical Editor.
767 Retrieved from <https://www.ncei.noaa.gov/sites/default/files/2020-04/woa18documentation.pdf>
768

769 Garzoli, S. L., & Gordon, A. L. (1996). Origins and variability of the Benguela Current. Journal
770 of Geophysical Research: Oceans, 101(C1), 897-906. doi:10.1029/95JC03221

771

772 Garzoli, S., Baringer, M., Dong, S., Perez, R. & Yao, Q. (2013), South Atlantic meridional
773 fluxes, Deep Sea Res., Part I, 71, 21–32. doi:10.1016/j.dsr.2012.09.003

774

775 Goes, M., Urban, N. M., Tonkonojekov, R., Haran, M., Schmittner, A., & Keller, K. (2010).

776 What is the skill of ocean tracers in reducing uncertainties about ocean diapycnal mixing and

777 projections of the Atlantic Meridional Overturning Circulation? Journal of Geophysical

778 Research: Oceans, 115(C12). doi:10.1029/2010JC006407

779

780 Goes, M., Wainer, I. & Signorelli, N. (2014). Investigation of the causes of historical changes in
781 the subsurface salinity minimum of the South Atlantic. Journal of Geophysical Research-Oceans,

782 119(9), 5654-5675. doi:10.1002/2014JC009812.

783

784 Goes, M., Goni, G., & Dong, S. (2015). An optimal XBT-based monitoring system for the South

785 Atlantic meridional overturning circulation at 34° S. Journal of Geophysical Research: Oceans,

786 120(1), 161-181. doi:10.1002/2014JC010202

787

788 Goes, M., Christophersen, J., Dong, S., Goni, G., & Baringer, M. O. (2018). An updated estimate

789 of salinity for the Atlantic ocean sector using temperature–salinity relationships. Journal of

790 Atmospheric and Oceanic Technology, 35(9), 1771-1784. doi:10.1175/JTECH-D-18-0029.1

791

792 Goes, M., Cirano, M., Mata, M. M., & Majumder, S. (2019). Long-Term Monitoring of the
793 Brazil Current Transport at 22° S From XBT and Altimetry Data: Seasonal, Interannual, and
794 Extreme Variability. *Journal of Geophysical Research: Oceans*, 124(6), 3645-3663.

795 doi:10.1029/2018JC014809

796

797 Goes, M., Murphy, L. N. & Clement, A.C. (2019b). The stability of the AMOC during Heinrich
798 events is not dependent on the AMOC strength in an Intermediate Complexity Earth System
799 model ensemble. *Paleoceanography and Paleoclimatology*, 34(8),1359-1374.

800 doi:10.1029/2019PA003580.

801

802 Goes, M., Goni, G., Dong, S., Boyer, T., & Baringer, M. (2020). The complementary value of
803 XBT and Argo observations to monitor ocean boundary currents and meridional heat and volume
804 transports: A case study in the Atlantic Ocean. *Journal of Atmospheric and Oceanic Technology*,
805 37(12), 2267-2282. doi:10.1175/JTECH-D-20-0027.1

806

807 Hernández-Guerra, A., Talley, L. D., Pelegrí, J. L., Vélez-Belchí, P., Baringer, M. O.,
808 Macdonald, A. M., & McDonagh, E. L. (2019). The upper, deep, abyssal and overturning
809 circulation in the Atlantic Ocean at 30 S in 2003 and 2011. *Progress in Oceanography*, 176,

810 102136. doi:10.1016/j.pocean.2019.102136

811

812 Herrford, J., Brandt, P., Kanzow, T., Hummels, R., Araujo, M., & Durgadoo, J. V. (2021).
813 Seasonal variability of the Atlantic Meridional Overturning Circulation at 11 S inferred from
814 bottom pressure measurements. *Ocean Science*, 17(1), 265-284. doi:10.5194/os-17-265-2021

815

816 Hersbach, H, Bell, B, Berrisford, P, et al. (2020). The ERA5 global reanalysis, *Q J R Meteorol*
817 *Soc.*, 146, 1999– 2049. doi:10.1002/qj.3803

818

819 Hummels, R., Brandt, P., Dengler, M., Fischer, J., Araujo, M., Veleda, D. & Durgadoo, J. V.
820 (2015), Interannual to decadal changes in the western boundary circulation in the Atlantic at
821 11°S, *Geophysical Research Letters*, 42(18), 7615-7622. doi:10.1002/2015GL065254.

822

823 Johns, W. E., Baringer, M. O., Beal, L. M., Cunningham, S. A., Kanzow, T., Bryden, H. L., ... &
824 Curry, R. (2011). Continuous, array-based estimates of Atlantic Ocean heat transport at 26.5 N.
825 *Journal of Climate*, 24(10), 2429-2449. doi:10.1175/2010JCLI3997.1

826

827 Kersalé, M., Meinen, C. S., Perez, R. C., Le Henaff, M., Valla, D., Lamont, T., et al. (2020).
828 Highly Variable Upper and Abyssal Overturning Cells in the South Atlantic, *Science Advances*,
829 6(32). doi:10.1126/sciadv.aba7573.

830

831 Koltermann, K.P., Gouretski, V.V. & Jancke, K. (2011). *Hydrographic Atlas of the World Ocean*
832 *Circulation Experiment (WOCE). Volume 3: Atlantic Ocean* (eds. M. Sparrow, P. Chapman and
833 J. Gould). International WOCE Project Office, Southampton, UK, ISBN 090417557X.

834

835 Koseki, S., Giordani, H., & Goubanova, K. (2019). Frontogenesis of the Angola–Benguela
836 frontal zone. *Ocean Science*, 15(1), 83-96. doi:10.5194/os-15-83-2019

837

- 838 Lee, J.-Y., Marotzke, J., Bala, G., Cao, L., Corti, S., Dunne, J.P., et al. (2021). Future Global
839 Climate: Scenario-Based Projections and Near- Term Information. In Masson-Delmotte, V.,
840 Zhai, P., Pirani, A., Connors, S.L., Péan, C., Berger, S., et al. (eds.), *Climate Change 2021: The*
841 *Physical Science Basis. Contribution of Working Group I to the Sixth Assessment Report of the*
842 *Intergovernmental Panel on Climate Change*. Cambridge University Press, Cambridge, United
843 Kingdom and New York, NY, USA, pp. 553–672. doi:10.1017/9781009157896.006
844
- 845 Lima, M. O., Cirano, M., Mata, M. M., Goes, M., Goni, G., & Baringer, M. (2016). An
846 assessment of the Brazil Current baroclinic structure and variability near 22° S in Distinct Ocean
847 Forecasting and Analysis Systems. *Ocean Dynamics*, 66(6), 893-916. doi:10.1007/s10236-016-
848 0959-6
849
- 850 Little, C. M., Piecuch, C. G., & Ponte, R. M. (2017), On the relationship between the meridional
851 overturning circulation, alongshore wind stress, and United States East Coast sea level in the
852 Community Earth System Model Large Ensemble. *J. Geophys. Res.*, 112, 4554–4568.
853 doi:10.1002/2017JC012713
854
- 855 Liu, M., & Tanhua, T. (2021). Water masses in the Atlantic Ocean: characteristics and
856 distributions. *Ocean Science*, 17(2), 463-486. doi:10.5194/os-17-463-2021
857
- 858 Locarnini, M. M., Mishonov, A. V., Baranova, O. K., Boyer, T. P., Zweng, M. M., Garcia, H. E.,
859 et al. (2018). *World ocean atlas 2018, volume 1: Temperature*. A. Mishonov, Technical Editor.

860 NOAA Atlas NESDIS 81, 52pp. Retrieved from
861 https://www.ncei.noaa.gov/sites/default/files/2020-04/woa18_voll.pdf
862

863 Lopez, H., Dong, S., Lee, S.-K., & Goni, G. (2016). Decadal Modulations of Interhemispheric
864 Global Atmospheric Circulations and Monsoons by the South Atlantic Meridional Overturning
865 Circulation. *J. Clim.*, 29(5), 1831-1851. doi:10.1175/JCLI-D-15-0491.1
866

867 Majumder, S., & Schmid, C. (2018). A study of the variability in the Benguela Current volume
868 transport, *Ocean Sci.*, 14, 273–283. doi:10.5194/os-14-273-2018.
869

870 Marcello, F., Tonelli, M., Ferrero, B., & Wainer, I. (2023). Projected Atlantic overturning slow-
871 down is to be compensated by a strengthened South Atlantic subtropical gyre. *Commun Earth
872 Environ.* 4, 92. doi:10.1038/s43247-023-00750-4
873

874 Mata, M. M., Cirano, M., Caspel, M. R. V., Fonteles, C. S., Gõni, G., & Baringer, M. (2012).
875 Observations of Brazil Current baroclinic transport near 22 S: variability from the AX97 XBT
876 transect. *Exchanges*, 58, 5-10.
877

878 McCarthy, G. D., Brown, P. J., Flagg, C. N., Goni, G., Houpert, L., Hughes, C. W., et al. (2020),
879 Sustainable Observations of the AMOC: Methodology and Technology, *Reviews of Geophysics*,
880 58(1). doi:10.1029/2019RG000654.
881

- 882 Meinen, C. S., Speich, S., Piola, A. R., Ansorge, I., Campos, E., Kersalé, M., et al. (2018).
883 Meridional overturning circulation transport variability at 34.5 S during 2009–2017: Baroclinic
884 and barotropic flows and the dueling influence of the boundaries. *Geophysical Research Letters*,
885 45, 4180-4188. doi:10.1029/2018GL077408
886
- 887 Pereira, J., Gabioux, M., Almeida, M. M., Cirano, M., Paiva, A. M., & Aguiar, A. L. (2014). The
888 bifurcation of the western boundary current system of the South Atlantic Ocean. *Brazilian*
889 *Journal of Geophysics*, 32(2), 241-257. doi:10.22564/rbgf.v32i2.456
890
- 891 Pita, I. I., Cirano, M., & Mata, M. M. (2020). An assessment of Brazil Current surface velocity
892 and associated transport near 22° S: XBT and altimetry data. *Regional Studies in Marine*
893 *Science*, 35, 101197. doi:10.1016/j.rsma.2020.101197
894
- 895 Polito, P. S., & Liu, W. T. (2003). Global characterization of Rossby waves at several spectral
896 bands. *Journal of Geophysical Research: Oceans*, 108(C1). doi:10.1029/2000JC000607
897
- 898 Pujol, M. I., Faugère, Y., Taburet, G., Dupuy, S., Pelloquin, C., Ablain, M., & Picot, N. (2016).
899 DUACS DT2014: the new multi-mission altimeter data set reprocessed over 20 years. *Ocean*
900 *Science*, 12(5), 1067-1090. doi:10.5194/os-12-1067-2016
901
- 902 Rahmstorf, S. (1996). On the freshwater forcing and transport of the Atlantic thermohaline
903 circulation. *Climate Dynamics*, 12(12), 799–811. doi:10.1007/s003820050144
904

905 Reid, J.L., 1989. On the total geostrophic circulation of the South Atlantic Ocean: Flow patterns,
906 tracers, and transports. *Prog. Oceanogr.* 23, 149–244. doi:10.1016/0079-6611(89)90001-3

907

908 Rhein, M. (2019). Taking a close look at ocean circulation. *Science*, 363(6426), 456-457.

909 doi:10.1126/science.aaw3111

910

911 Roemmich, D. & Gilson, J. (2009) The 2004-2008 mean and annual cycle of temperature,

912 salinity, and steric height in the global ocean from the Argo Program. *Progress in Oceanography*,

913 82, 81-100. doi:10.1016/j.pocean.2009.03.004

914

915 Roemmich, D., Johnson, G.C., Riser, S., Davis, R., Gilson, J., Owens, W.B., Garzoli, S.L.,

916 Schmid, C., & Ignaszewski, M. (2009). The Argo Program: Observing the global ocean with

917 profiling floats. *Oceanography*, 22(2), 34–43. doi:10.5670/oceanog.2009.36.

918

919 Stommel, H. (1961), Thermohaline Convection with Two Stable Regimes of Flow, *Tellus*, 13(2),

920 224-230. doi:10.1111/j.2153-3490.1961.tb00079.x.

921

922 Stramma, L., & England, M. (1999). On the water masses and mean circulation of the South

923 Atlantic Ocean. *Journal of Geophysical Research: Oceans*, 104(C9), 20863-20883.

924 doi:10.1029/1999JC900139

925

- 926 Stramma, L., Kieke, D., Rhein, M., Schott, F., Yashayaev, I., & Koltermann, K. P. (2004). Deep
927 water changes at the western boundary of the subpolar North Atlantic during 1996 to 2001, *Deep*
928 *Sea Res.*, 51, 1033–1056. doi:10.1016/j.dsr.2004.04.001
- 929
- 930 Strub, P. T., James, C., Combes, V., Matano, R. P., Piola, A. R., Palma, E. D., et al. (2015).
931 Altimeter-derived seasonal circulation on the southwest Atlantic shelf: 27°–43° S. *Journal of*
932 *Geophysical Research: Oceans*, 120(5), 3391-3418. doi:10.1002/2015JC010769.
- 933
- 934 Talley, L. D. (2011). *Descriptive physical oceanography: an introduction*. Academic press. 6th
935 ed, pp. 560.
- 936
- 937 Todd, R. E., Chavez, F. P., Clayton, S., Cravatte, S., Goes, M., Graco, M., et al. (2019). Global
938 perspectives on observing ocean boundary current systems. *Frontiers in Marine Science*, 6(423).
939 doi: 10.3389/fmars.2019.00423.
- 940
- 941 Veitch, J. A., Florenchie, P., & Shillington, F. A. (2006). Seasonal and interannual fluctuations
942 of the Angola–Benguela Frontal Zone (ABFZ) using 4.5 km resolution satellite imagery from
943 1982 to 1999. *International Journal of Remote Sensing*, 27(05), 987-998.
944 doi:10.1080/01431160500127914
- 945
- 946 Volkov, D. L., Baringer, M., Smeed, D., Johns, W., & Landerer, F. W. (2019). Teleconnection
947 between the Atlantic meridional overturning circulation and sea level in the Mediterranean Sea.
948 *Journal of climate*, 32(3), 935-955. doi:10.1175/JCLI-D-18-0474.1

949

950 Weijer, W., Cheng, W., Drijfhout, S. S., Fedorov, A. V., Hu, A., Jackson, L. C., et al. (2019).

951 Stability of the Atlantic meridional overturning circulation: A review and synthesis. *Journal of*

952 *Geophysical Research: Oceans*, 124(8), 5336–5375. doi:10.1029/2019JC015083

953

954 Zweng, M. M., Seidov, D., Boyer, T. P., Locarnini, M., Garcia, H. E., Mishonov, A. V., et al.

955 (2019). *World ocean atlas 2018, volume 2: Salinity*. A. Mishonov, Technical Editor, NOAA

956 Atlas NESDIS 82, 50pp. Retrieved from <https://www.ncei.noaa.gov/sites/default/files/2022->

957 06/woa18_vol2.pdf